

The influence of bathymetry over circulation on the Amundsen Sea continental shelf

Michael Haigh¹, Paul Holland¹, and Adrian Jenkins²

¹British Antarctic Survey

²BAS

December 7, 2022

Abstract

Ice sheets such as Pine Island and Thwaites Glaciers which terminate at their ice shelves in the eastern Amundsen Sea, West Antarctica, are losing mass faster than most others about the continent. The mass loss is due to basal melting, this affected by a deep current thought to be guided by bottom bathymetry that transports warm Circumpolar Deep Water (CDW) from the continental shelf break towards the ice shelves. This current and associated heat transport are controlled by the near-surface winds that vary on a range of timescales due to both anthropogenic and natural effects. In this study we use idealised models to reproduce essential features of the Amundsen Sea circulation and heat transport. The aim is to elucidate the role of bathymetric features in shaping the circulation and in enabling heat transport from the deep ocean onto the continental shelf. Bathymetric variations along the continental slope enhance on-shelf heat transport by inducing breaks in the Antarctic Slope Front that separates off-shelf CDW from the colder, fresher shelf waters. The idealised model results imply that a ridge that blocks deep westward inflow from the Bellingshausen Sea leads to the existence of a deep cyclonic circulation on the shelf. Part of this circulation is an eastward undercurrent that flows along the continental shelf break. The broader cyclonic circulation transports heat that has been recently fluxed onto the shelf towards the south. These fundamental investigations will help refine the aims of future fieldwork and modelling.

The influence of bathymetry over circulation on the Amundsen Sea continental shelf

Michael Haigh¹, Paul R. Holland¹ & Adrian Jenkins²

¹British Antarctic Survey, Cambridge, UK.

²Department of Geography and Environmental Sciences, Northumbria University, Newcastle
upon Tyne, UK

Abstract

Ice sheets such as Pine Island and Thwaites Glaciers which terminate at their ice shelves in the eastern Amundsen Sea, West Antarctica, are losing mass faster than most others about the continent. The mass loss is due to basal melting, this affected by a deep current thought to be guided by bottom bathymetry that transports warm Circumpolar Deep Water (CDW) from the continental shelf break towards the ice shelves. This current and associated heat transport are controlled by the near-surface winds that vary on a range of timescales due to both anthropogenic and natural effects. In this study we use idealised models to reproduce essential features of the Amundsen Sea circulation and heat transport. The aim is to elucidate the role of bathymetric features in shaping the circulation and in enabling heat transport from the deep ocean onto the continental shelf. Bathymetric variations along the continental slope enhance on-shelf heat transport by inducing breaks in the Antarctic Slope Front that separates off-shelf CDW from the colder, fresher shelf waters. The idealised model results imply that a ridge that blocks deep westward inflow from the Bellingshausen Sea leads to the existence of a deep cyclonic circulation on the shelf. Part of this circulation is an eastward undercurrent that flows along the continental shelf break. The broader cyclonic circulation transports heat that has been recently fluxed onto the shelf towards the south. These fundamental investigations will help refine the aims of future fieldwork and modelling.

Plain language summary

The ice sheets that float on the waters in the eastern Amundsen Sea, West Antarctica, are losing mass faster than most others about the continent. Relatively warm ocean waters have access to the undersides of these ice shelves, and are thought to be the cause of the great mass loss. It is understood that deep currents transport warm waters from the deep ocean in the north towards the Antarctic coast in the south. However, the details of such currents are not known. Complicated regional models, which simulate the physics in the Amundsen Sea region, have been useful to help researchers understand the involved physical processes. In this study we use a sequence of simpler models to develop a more fundamental understanding of these processes. In particular, these simple models allow us to thoroughly investigate the role that ocean floor bathymetry plays in determining the flows in the region.

Key Points:

- Idealised models are used to reproduce essential features of the Amundsen Sea circulation.
- A deep cyclonic circulation exists in the eastern Amundsen Sea because of sufficient blocking of deep flow by zonal boundaries and a ridge.
- This cyclonic circulation enables greater on-shelf heat transport and efficiently transports heat shoreward.

1 Introduction

The ice streams that drain into the Amundsen Sea, West Antarctica, are losing mass faster than most others about the continent [Rignot et al., 2008, Shepherd et al., 2018]. In particular, Pine Island Glacier and Thwaites Glacier are identified as two major mass sinks for the West Antarctic Ice Sheet [Pritchard et al., 2012, Mouginot et al., 2014, Rignot et al., 2014, Joughin et al., 2014]. Such great mass loss is due to the access that warm Circumpolar Deep Water (CDW), which is $\sim 3^\circ\text{C}$ above the local freezing point, has to the bases of the floating ice shelves [Jacobs et al., 1996, Walker et al., 2007, Dutrieux et al., 2014, Heywood et al., 2016]. Concerns for the region are intensified due to the bottom topography at the grounding lines of the ice shelves that deepens shoreward, a configuration associated with the potential marine ice sheet instability [Favier et al., 2014, Joughin et al., 2014].

In many sections around Antarctica, warm and salty CDW is excluded from the continental shelf and the ice shelves by the Antarctic Slope Front (ASF) at the continental slope. The ASF separates the CDW from fresher, cooler waters above and to the south [Ou, 2007, Stewart and Thompson, 2013, Stewart et al., 2019] and is maintained (at least partially) by coastal easterlies that drive downwelling at the Antarctic coast that pushes down isopycnals [Jacobs, 1991, Jacobs et al., 2012, Jenkins et al., 2016, Thompson et al., 2018]. A compensating sea-surface height gradient of opposite sign at the surface means that the ASF is commonly associated with a westward surface current which weakens with depth, possibly with an absolute eastward undercurrent near the ocean bottom. While there are observations [Walker et al., 2007, 2013] and model diagnoses [Dotto et al., 2019, Webber et al., 2019] of an ASF at the Amundsen Sea continental slope, this is weaker than in most other regions around Antarctica [Thompson et al., 2018]. A variety of mechanisms can contribute to the weaker ASF in the Amundsen Sea, including the weak and variable surface wind patterns [Raphael et al., 2016], frequent cross-shelf eddy intrusions [Klinck and Dinniman, 2010] and the lack of dense shelf water formation in the region [Petty et al., 2013, Thompson et al., 2018]. With a weaker ASF, CDW floods the continental shelf in the Amundsen Sea region, and therefore has great access to the ice shelves, contributing to the large melt rates in the region.

The undercurrent also plays a role in getting heat on the shelf, after being guided shoreward by troughs that cut the shelf break. However, a precise understanding of this feature is lacking. The observations of Walker et al. [2013] suggest a deep eastward current hugs the northernmost section of the continental shelf and the upper section of the shelf slope. This current turns southward when it encounters a trough near 114°W (see figures 1 and 2 for large-scale and finer-scale illustrations of the bathymetry in the region), transporting warm CDW across the shelf break. The fate of this deep current or its consistency is not certain given the spatially and temporally limited extent of the data. Numerical model results [Thoma et al., 2008, Kimura et al., 2017, Webber et al., 2019, Dotto et al., 2020] suggest this warm current, guided by bathymetry, turns back to the east and makes a second southward turn in the eastern section of the eastern Amundsen Sea (near 105°W)

73 before continuing towards the ice shelves.

74 The deep current and the thickness of the on-shelf CDW layer are highly variable across a range of timescales.
75 In particular, decadal variability in the deep current and CDW layer thickness, which are linked to variability
76 in the wind forcing [Thoma et al., 2008, Dutrieux et al., 2014, Kimura et al., 2017], leads to decadal variability
77 in basal melting [Jenkins et al., 2018]. In addition Holland et al. [2019] suggest that a climatic westerly trend
78 in the shelf break winds has led to periods of stronger eastward flow in recent decades, potentially enhancing
79 the transport of warm CDW towards the ice shelves and accelerating melting. Ice-ocean simulations presented
80 by Naughten et al. [2022] add evidence to the notion that warming and accelerated melting in the Amundsen
81 Sea over the last century are driven by anthropogenic changes to the shelf break winds and the associated
82 effects on the eastward undercurrent (see their figure 2). However, more recent work by Holland et al. [2022]
83 found that significant trends are limited to the deep ocean, where the westerlies have been intensifying due to
84 anthropogenic effects [Arblaster and Meehl, 2006, Gillett et al., 2013, Goyal et al., 2021].

85 Many studies discuss the essential features of the Amundsen Sea circulation and heat transport. Such studies
86 commonly utilise either (sparse) observations [Walker et al., 2007, 2013, Assmann et al., 2013] or regional models
87 [Thoma et al., 2008, Donat-Magnin et al., 2017, Kimura et al., 2017] that typically include many physical
88 processes and detailed configurations. The regional models can be useful for gaining an understanding of the
89 Amundsen Sea’s past, present and future. However, interpreting and explaining model outputs can be difficult
90 due to the large number of interacting processes that act across many timescales. In addition, since regional
91 models are computationally expensive, it is difficult to determine the dependencies of the models’ outputs on
92 factors such as boundary/initial conditions, model forcings, domain geometries and parameter choices. This
93 motivates the use of reduced-complexity idealised models.

94 In this study we progressively develop an idealised model of the eastern Amundsen Sea to improve our
95 understanding of the essential present-day dynamics captured in a companion regional model and observed in
96 the real world. In particular, we will examine the roles that winds and bottom bathymetry play in shaping
97 the Amundsen Sea circulation and in transporting heat towards the ice shelves. The intention is that this will
98 allow for more confident predictions of the fate of the Amundsen Sea and its ice shelves. It is also anticipated
99 that the results of this study will help to refine the aims of future fieldwork and modelling investigations.

100 This study is organised as follows. In section 2 we describe the output from a realistic regional model of the
101 Amundsen Sea. This will represent a benchmark to which idealised model results can be compared. In section
102 3.1 we introduce the most basic setup of the idealised model and describe the wind, temperature and salinity
103 forcing regimes. Through section 3.2 we progressively adapt the bathymetry to roughly reproduce certain
104 bathymetric features in the regional model, and we discuss their influence in the resulting flow responses. Then
105 in section 3.3 we discuss the heat transport across the shelf break in these simulations, focusing on the role of
106 bathymetric features. Next, in section 3.4 we consider the effects of simple changes to the wind forcing. Lastly,
107 in section 4 we summarise our results and discuss their relationship with the real world.

2 Regional model

2.1 Model details

For the regional model we use checkpoint 65s of the Massachusetts Institute of Technology general circulation model (MITgcm) in an Amundsen Sea configuration similar to that of Kimura et al. [2017] and Bett et al. [2020]. This is also the same model and configuration used by Naughten et al. [2022], with one minor difference in the fixed iceberg flux field. The model domain extends from 140°W to 80°W and from 75.5°S to 62°S. The lateral grid resolution is 0.1° in longitude, such that the isotropic grid step is ~ 2.75 km in the south of the domain and ~ 5.15 km in the north. The vertical direction is discretised by 50 levels with the thinnest (10 m) levels near the surface and the thickest (200 m) levels near the ocean bottom.

Lateral viscosity is represented using the Leith scheme in the horizontal and a constant Laplacian viscosity is used in the vertical. Vertical diffusion of potential temperature θ and salinity S is parameterised using the K-profile parameterisation scheme [Large et al., 1994], while there is no explicit lateral diffusion of θ and S . Ice shelves and sea ice provide interactive sources and sinks of freshwater. A free-slip condition is applied at the lateral boundaries and quadratic bottom friction is applied at the ocean floor.

The model is forced by six-hourly ERA5 10 m winds, precipitation, surface long-wave and short-wave radiation, 2 m air temperature and specific humidity, and atmospheric pressure. Open boundary conditions in the west, north and east are derived from the World Ocean Atlas for salinity and potential temperature. For the ocean velocities and sea ice properties the boundary conditions are derived from the Southern Ocean State Estimate. The model is spun up using the 1979-2002 interval of the external forcing data. After this spinup, forcing is restarted from 1979, the beginning of the analysis period of the regional model. All data that we present are obtained by averaging outputs between January 1979 and December 2011.

Figure 1 shows the time-mean surface stress with sea ice accounted for. Also shown is the bottom bathymetry and the outline of the eastern Amundsen Sea region in which we focus our attention in this study. Surface stresses are typically eastward to the north of the continental slope and westward to the south of the continental slope. Along the continental slope the surface stress is close to zero, but the stress curl is strongly cyclonic, corresponding to upwelling velocities.

In figure 2 we show the bathymetry (colour) in the eastern Amundsen Sea. In figure 2a four bathymetric features are highlighted (red dots), that we identify as being particularly important for the oceanography of the eastern Amundsen Sea. These are the Pine Island-Thwaites West (PITW) trough, the deep central basin (C), the Pine Island-Thwaites East trough (PITE) and the ridge (R). Many studies have discussed the importance of the troughs and basin (sometimes also referred to as a trough), but not the ridge. The ridge is more easily visible as the tongue of masked bathymetry in figure 2b stretching from the coast to the shelf break near 101°W.

In our Bedmachine topography [Morlighem, 2020], the ridge is of approximately 400 m depth and lies to the west of similarly shallow topographic features between the Amundsen and Bellingshausen Seas. While the ridge blocks deep inflow from the east, some deep inflow is also blocked upstream in the Bellingshausen Sea. The ridge is also visible in the RTopo-1 data set of Timmermann et al. [2010] and the more recent IBCSO v2 dataset [Dorschel et al., 2022]. We highlight, though, that there is great uncertainty regarding the actual topography on the continental shelf between the Bellingshausen and Amundsen Seas due to a significant lack of data. In the above datasets, the topography in this region is predicted using a combination of statistical

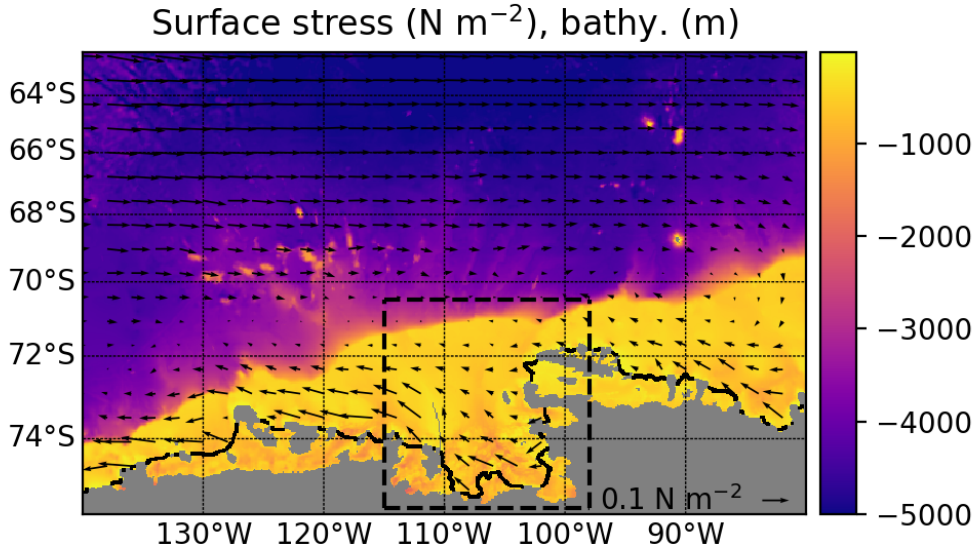


Figure 1: Time-mean (1979-2011) surface stress (arrows) accounting for sea ice, used to force the regional model. Colour represents the bottom bathymetry (units m). The dashed box outlines the eastern Amundsen Sea, in which we will focus our attention. Grey masking represents land and the solid black contour represents the edge of the floating ice shelves at the ocean surface.

147 methods and nearby measurements. Nonetheless, the ridge is present in the topographic datasets cited above
 148 and as a result is present in realistic simulations of the area. However, its role in shaping the circulation in
 149 these simulations and the real Amundsen Sea is little discussed.

150 2.2 Model output

151 In this section we describe the output of the regional model, with some brief explanations of the involved
 152 physical mechanisms. Further details of the mechanisms will be given when considering the idealised model.

153 Figure 2a shows the time-mean near-surface (depth $z = -5$ m) flow and potential temperature in the
 154 eastern Amundsen Sea. Near the surface, cold and fresh waters enter the eastern Amundsen Sea from the
 155 Bellingshausen Sea via the narrow shelf region bounded to the south by the coast and to the north by the
 156 continental shelf break. The current then turns southward and cyclonically traverses the eastern Amundsen
 157 Sea before exiting in the west towards the Dotson Ice Shelf. Surface stratification (vertical gradient in salinity)
 158 makes it possible for the surface flow to pass over the deep central basin, rather than be blocked by it.

159 The primary reason for the surface current following the coast is the southward Ekman transport caused
 160 by the westward surface stresses that create a shoreward sea surface height gradient along the coast. It is also
 161 possible that the surface current is partially guided by the strong gradient in the bottom bathymetry present
 162 along much of the coast, but the surface stratification will weaken this connection. This surface current is
 163 often referred to as the Antarctic Coastal Current (AACC) [Moffat et al., 2008, Schubert et al., 2021]. Another
 164 current is the Antarctic Slope Current (ASC) [Chavanne et al., 2010, Dong et al., 2016] which is locked to the
 165 continental slope, but is thought to have a weak signal in the real Amundsen Sea [Thompson et al., 2020], as
 166 is the case in the regional model output.

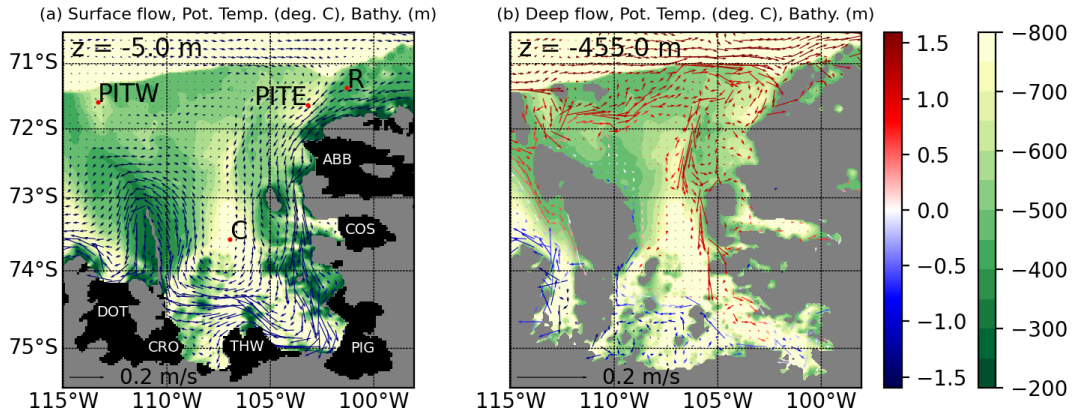


Figure 2: (a) The surface (depth $z = -5$ m) time-mean flow (arrows) and potential temperature (arrow colour, deg. C) in the eastern Amundsen Sea. (b) The deep ($z = -455$ m) time-mean flow and potential temperature in the eastern Amundsen Sea. In both panels, the background colour depicts the bottom bathymetry and grey masking represents land. In panel (a) black masking represents the ice shelves. Labeled are the Dotson, Crosson, Thwaites, Pine Island Glacier, Cosgrove and Abbot ice shelves. Also in panel (a) are four red dots are placed at important bathymetric features. These are the Pine Island-Thwaites West (PITW) trough, the central basin (C), the Pine Island-Thwaites East (PITE) trough and the ridge (R).

167 Figure 2b shows the time-mean deep ($z = -455$ m) flow and potential temperature. The deep flow consists
 168 of a warm current that circulates the eastern Amundsen Sea cyclonically. Since the ridge blocks deep inflow
 169 from the east, waters for this circulation are predominantly sourced from an eastward undercurrent in the
 170 west that travels along the continental slope and turns onto the shelf via the PITW trough. This is similar
 171 to the observations of Assmann et al. [2013] and Walker et al. [2013]. A similar process occurs at the PITE
 172 trough, although the time-mean currents onto the shelf are less coherent. The PITW trough is connected to
 173 the PITE trough by relatively shallow east-west oriented geostrophic f/h (Coriolis frequency / water column
 174 depth) contours, along which the current travels after entering the PITW trough. Once reaching the PITE
 175 trough, the current is blocked by the f/h contours of the trough and turns southward; we emphasise that the
 176 current does not travel into the trough, but rather along its flank. The current then passes by the eastern side
 177 of the central basin and continues towards the ice shelves.

178 As the deep current circulates by the coast and the floating ice shelves it entrains cold fresh meltwater and
 179 becomes more buoyant. This causes the current to shoal and permits it to move above bottom topography that
 180 is shallower than the upstream southward-flowing current ($z = -455$ m for the level shown). The outflowing
 181 deep current (not visible in figure 2b) then follows roughly the same bathymetric contours (Bear Ridge) as the
 182 near-surface current, which guide it out of the eastern Amundsen Sea.

183 Here we have described the main features of the time-mean (1979-2011) surface and deep currents in the
 184 eastern Amundsen Sea. Naturally, these currents are highly variable over a range of timescales. As an example,
 185 at some instances in time both the deep and depth-integrated flows in the eastern Amundsen Sea feature a
 186 closed cyclonic circulation, but this is not strong enough to have a signal in the time mean. Our focus is on
 187 the mean circulation with the intention that this will aid future investigations into deviations from this mean.

188 Figure 3a shows the time-mean $\theta = -0.5^\circ\text{C}$ isotherm depth in the eastern Amundsen Sea. This illustrates

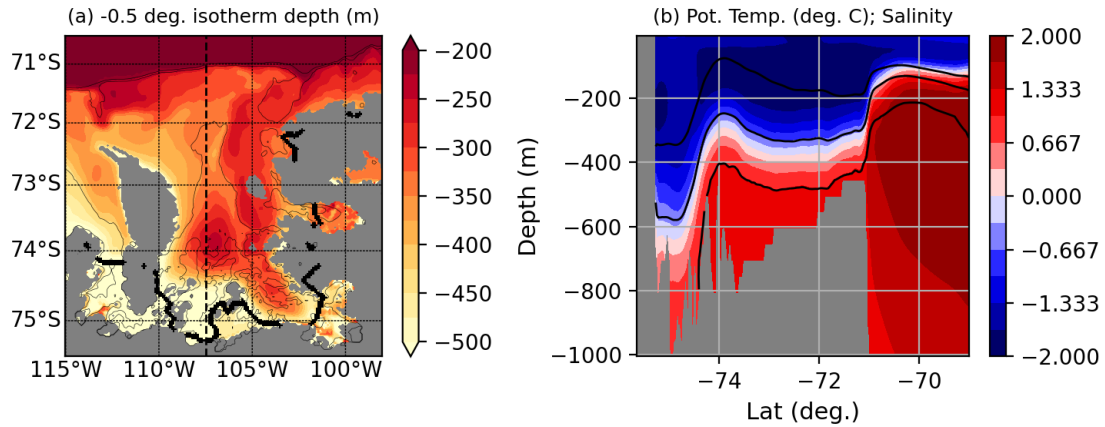


Figure 3: (a) The time-mean -0.5 deg. C isotherm depth (m). Grey areas represent land or locations where the isotherm doesn't exist. The thin black contours represent the -1000 m and -600 m bathymetric contours. The thick black contour represents the fronts of the ice shelves. (b) A latitude-depth slice of the time-mean potential temperature at 107.5°W , the longitude depicted by the dashed line in (a). The black lines are the 34.3 g/kg, 34.5 g/kg and 34.7 g/kg salinity contours, with the lower salinities nearer the surface.

189 the access that warm CDW has to the continental shelf, and is very similar to the model results of Webber
 190 et al. [2019]. The isotherm is relatively shallow to the east of the central basin, with a warm tongue extending
 191 from the shelf break to the ice shelves. Comparing with figure 2b, the role of the deep flow in transporting heat
 192 southwards from the shelf break is clear. However, the mechanisms that transport CDW from the open ocean
 193 onto the continental shelf are less clear. Figure 2b implies that simple onshore advection by the mean current
 194 through the PITW trough is one possible mechanism. The connectedness of the shallow $\theta = -0.5^\circ\text{C}$ isotherm
 195 from the shelf break via the PITE trough to the south suggests the PITE trough is important for on-shelf heat
 196 transport.

197 Other mechanisms such as eddy intrusions, upwelling in bottom Ekman layers or transient wind-driven
 198 intrusions [Klinck and Dinniman, 2010] are other possible candidates. Like with the circulation the isotherm
 199 depth is subject to temporal variability on a range of timescales. Of particular relevance to this study is
 200 variability due to wind fluctuations [Thoma et al., 2008, Kimura et al., 2017].

201 The location of the Antarctic slope front (ASF) is illustrated in figure 3a by the southward deepening of
 202 the isotherm along the continental slope. The latitude-depth slice of the time-mean potential temperature θ at
 203 107.5°W in figure 3b shows the ASF in finer detail. The salinity S contours plotted in figure 3b confirm the
 204 ASF is a front in all three of potential temperature, salinity and density. In many sections around Antarctica
 205 the ASF intersects the continental shelf or slope [Thompson et al., 2018], but in the Amundsen Sea the ASF is
 206 weaker and CDW floods the lower section of the on-shelf water column.

3 Idealised model

3.1 Model details

For the idealised model we use the same MITgcm 65s checkpoint, but in a greatly simplified configuration. The domain is a zonally periodic channel of side length 600 km in the zonal direction and 500 km in the meridional direction. We use an f -plane domain with reference Coriolis parameter $f_0 = -1.4 \times 10^{-4} \text{ s}^{-1}$, corresponding to a reference latitude of 74.27°S . The domain is discretised onto a uniform $N_x \times N_y = 240 \times 200$ grid, corresponding to a lateral grid resolution of 2.5 km. The vertical direction is discretised by 50 levels each 20 m thick. As in the regional model, free-slip boundary conditions are applied at the walls and quadratic bottom friction is applied at the ocean floor.

The model is initially set up with a continental shelf domain, with shallower (500 m depth) waters in the south and deeper (1000 m depth) waters in the north, as shown in figure 4a. Off-shelf, the real Amundsen Sea is much deeper, but the weak communication between off-shelf deep waters and on-shelf waters means modelling the very deep off-shelf flow is not necessary. This simple bathymetry will be progressively increased in complexity until the main features of the real Amundsen Sea are represented.

Also shown in figure 4a is the steady, zonally uniform cosine-shaped zonal wind stress used to force these models. The wind stress is eastward in the north, with a maximum stress of 0.025 N m^{-2} at the northern boundary, and westward in the south, with a minimum stress of -0.025 N m^{-2} at the southern boundary. The wind stress at the centre of the continental slope is zero, at which point the wind stress curl (which is cyclonic everywhere) is maximised. This wind stress profile and magnitude are intended to reproduce the surface stress curl and upwelling/downwelling velocities associated with the mean surface stresses in the regional model (figure 1). In section 3.4 we consider a different wind profile motivated by predicted changes to the winds in the Amundsen Sea region.

The entire domain is initialised with zero flow, potential temperature $\theta = -1.8^\circ\text{C}$ and salinity $S = 33.5 \text{ g/kg}$. These choices for θ and S represent cold and fresh initial conditions. Potential temperature θ and salinity S are forced by a relaxation with a 10-day timescale at the northern boundary to the profiles shown in figure 4b (solid lines). These profiles are motivated by observations in the region [Arneborg et al., 2012, Assmann et al., 2013, Dutrieux et al., 2014, Walker et al., 2007, 2013] and output from the regional model. The prescribed pycnocline is between 200 m and 340 m depth, throughout which the temperature and salinity both increase linearly with depth. This pycnocline separates cold fresh ($\Theta = -1.8^\circ\text{C}$, $S = 33.5 \text{ g/kg}$) surface waters from warm salty ($\theta = 1^\circ\text{C}$, $S = 34.5 \text{ g/kg}$) CDW at depth.

The relaxation in the north is the only source of CDW for the idealised model. Therefore, by forcing the model in this way and by using the cold fresh initial conditions we guarantee that the only source for on-shelf CDW is southward advection across the continental shelf break. This is useful given our aim to study the role of winds and bathymetry in controlling access of CDW to the continental shelf in the eastern Amundsen Sea.

At the southern boundary θ and S are relaxed with a relaxation timescale of 100 days back to their cold and fresh initial conditions. This additional weak buoyancy forcing is necessary to maintain a realistic on-shelf heat distribution in steady state. That is, because the idealised model does not include any thermodynamic forcings such as ice shelf melt, sea ice melt and surface fluxes, the continental shelf in the idealised model becomes too warm without an additional mechanism for removing heat from the shelf. Simulations without

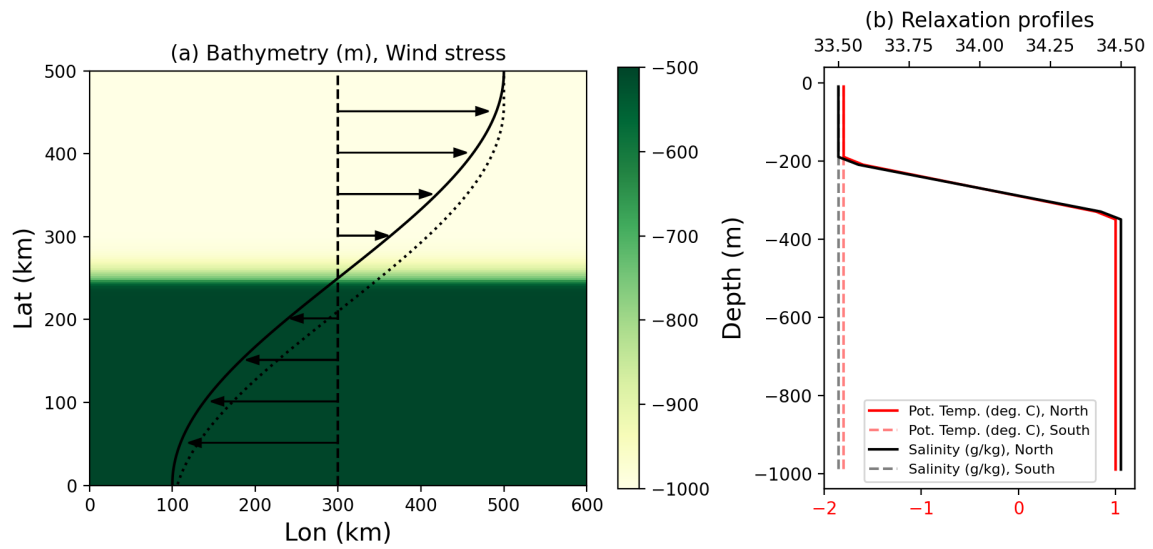


Figure 4: (a) The continental shelf bottom bathymetry used in the idealised model (in colour). This basic bottom bathymetry will be progressively updated. The solid curve and arrows represent the steady, zonally uniform wind stress profile which has a maximum absolute stress of 0.025 N m^{-2} attained at the northern and southern boundaries. The dashed line represents zero wind stress. The dotted curve is the original wind stress profile translated south by 40 km, used in section 3.4. (b) The relaxation profiles versus depth for potential temperature (red, deg. C) and salinity (black, g/kg). Solid lines represent the profiles for the northern boundary and dashed lines are for the southern boundary.

246 relaxation in the south (not shown) confirm this to be true, but we emphasise that the flow fields in these
247 simulations are qualitatively similar to the flow fields in the simulations with the southern relaxation. That the
248 weak southern relaxation is required to achieve a realistic on-shelf heat distribution highlights the importance
249 of ice shelf melt, sea ice melt and surface fluxes to the thermodynamic balance in the real world and regional
250 model. The relaxations imposed at the southern and northern boundaries are tapered to zero over a range of
251 four grid points inward from the boundary.

252 The model includes vertical ($10^{-3} \text{ m}^2 \text{ s}^{-1}$) and horizontal ($10 \text{ m}^2 \text{ s}^{-1}$) viscosity and weak biharmonic
253 diffusion (non-dimensional grid-dependent biharmonic viscosity of 0.1) to ensure model stability. Potential
254 temperature and salinity are subject to vertical diffusion ($10^{-5} \text{ m}^2 \text{ s}^{-1}$) but no horizontal diffusion. Because
255 of the linearity of the advection-diffusion equation and the linear equivalence of the θ/S initial conditions
256 and relaxation profiles, θ and S are mathematically equivalent. This means that the salinity and density
257 distributions at any time in the simulation can be inferred from the temperature distribution and vice-versa.
258 The simulation outputs that we show are after 30 years of model runtime, sufficient for the flow, temperature
259 and salinity fields to have reached equilibrium.

260 3.2 Flow responses

261 3.2.1 Zonally uniform case

262 We first present model output for the zonally uniform case described in the previous section. In this case all
263 results are approximately zonally uniform on lengthscales larger than the mesoscale eddy scale. Figure 5a shows
264 the zonal-mean sea surface height (SSH) anomaly averaged over the final year of a 30-year simulation. The V-
265 shaped SSH profile is the consequence of southward wind-driven Ekman transport in the south and northward
266 transport in the north, which creates a convergence of mass at the southern and northern boundaries.

267 Figure 5b shows the zonal-mean, time-mean zonal velocity (colour) and potential temperature (contours).
268 The difference between the warm northern and cold southern relaxations creates a net-southward deepening
269 of the isotherms. This southward deepening is also contributed to by Ekman downwelling at the southern
270 boundary that pushes down on-shelf isopycnals and forces CDW off the shelf [Jacobs, 1991, Jenkins et al.,
271 2016]. That the relaxation is stronger at the northern boundary compared to the southern boundary means
272 Ekman downwelling has a relatively strong effect in the south compared to the north. In the real ocean and
273 regional model, there is no northern boundary so close to the shelf break. However, the effects of the Ekman
274 downwelling at the northern boundary in the idealised model are suppressed by the relatively strong relaxation.

275 The northward gradient in potential temperature – which exists also in salinity and density – becomes
276 concentrated at the continental slope, forming an ASF. The ASF forms in this way because baroclinic instability
277 is suppressed over the continental slope, this due to the overwhelming contribution to the meridional potential
278 vorticity gradient Q_y by the rapidly changing bottom bathymetry [Chen and Kamenkovich, 2013, Chen et al.,
279 2020] (baroclinic instability requires a change in the sign of Q_y in the vertical direction). This prevents
280 baroclinic eddies from being excited over the continental slope, but not over flat-bottomed areas of the domain.
281 Therefore, while baroclinic eddies act to flatten the isotherms (and isopycnals) over the flat-bottomed areas of
282 the ocean, this effect is suppressed over the continental slope so the sharp ASF persists. At times the ASF
283 can be sufficiently steep such that the potential vorticity gradient created by the lateral density gradient is
284 large enough to cancel with the contribution from the bottom slope. At such instances baroclinic eddies can be

285 generated, leading to a weakening of the ASF and restoration of stability. This reasoning also implies that the
286 ASF will have a tendency to be steeper in regions of Antarctica where the continental shelf slope is steeper.

287 The flow is typically eastward in the north and westward in the south, and is strongly barotropic apart from
288 at the continental slope because of the ASF. Although the ASF causes the flow at the continental slope to be
289 more eastward with depth (via the thermal wind relation), this effect is only strong enough to produce a weak
290 eastward flow on the upper section of the continental slope and does not lead to a strong eastward undercurrent
291 along the shelf break. This is in contrast to the regional model that has strong eastward flow along much of
292 the shelf break (mainly upstream of the troughs), as visible in figure 2b.

293 Above the ASF there is a fast westward current, consistent with the strong southward SSH gradient at the
294 same latitudes. That this westward current exists above the ASF could be interpreted as the reason for the
295 weak eastward undercurrent. However, it is more accurate to say the weak eastward undercurrent relative to
296 the regional model is due to the zonal symmetry and periodicity of the idealised model. In such a model, there
297 is a lack of mechanisms for meridional transfer of zonal momentum, which means that any zonal momentum
298 imparted at the surface by the wind stress must be removed at the ocean bottom via bottom friction at the
299 same latitude. Therefore, the zonal flow near the ocean floor is dictated by the winds, as it must generate the
300 bottom friction that opposes the wind stress. This is confirmed by plots of the surface and bottom stresses (not
301 shown). This is not an exact balance because the model includes lateral viscosity and the flow features non-zero
302 time-mean meridional overturning Ekman flow. However, the weakness of the viscosity and the Ekman flow
303 means they make negligible contributions to the zonal-mean zonal momentum budget. We conclude that the
304 westward surface current (and associated SSH gradient) must exist to compensate for the ASF: without the
305 strong westward surface current, the deep eastward flow would be too strong and too much eastward momentum
306 would be removed by bottom friction at these latitudes.

307 A consequence of the deep flow being approximately set by the surface stress is that changes in the θ and S
308 relaxation (e.g., adjusting the pycnocline height) will change the SSH gradient and surface flow in the balanced
309 flow response, but cannot notably change the deep flow. For example, shifting the pycnocline downwards in
310 the relaxation profiles will reduce the net height change in the ASF at the continental slope, which means that
311 above the ASF the southward SSH gradient and westward surface current must weaken in order for the same
312 velocities to be realised at the ocean floor (thus providing the bottom stress required to balance the surface
313 stress).

314 If the idealised model were instead forced by a wind with associated stress that accounted for the surface
315 flow (like in the regional model), then the adjustment of the surface flow as a result of changes to the pycnocline
316 would alter the stress at the ocean's surface. This implies that in this case the deep flow need not be the same
317 under alterations to the pycnocline. However, given that near-surface winds are typically much faster than the
318 ocean's surface flow, making this alteration to the winds means that even in this case the deep flow would still
319 be predominantly determined by the surface winds.

320 **3.2.2 Adding walls to the continental shelf**

321 We now add walls to the continental shelf to create an area similar to the eastern Amundsen Sea. The off-shelf
322 dynamics do not change in any notable way since this part of the domain is not changed. On-shelf, however,
323 the inclusion of walls leads to the zonal blockage of a large range of f/h contours, meaning that velocity

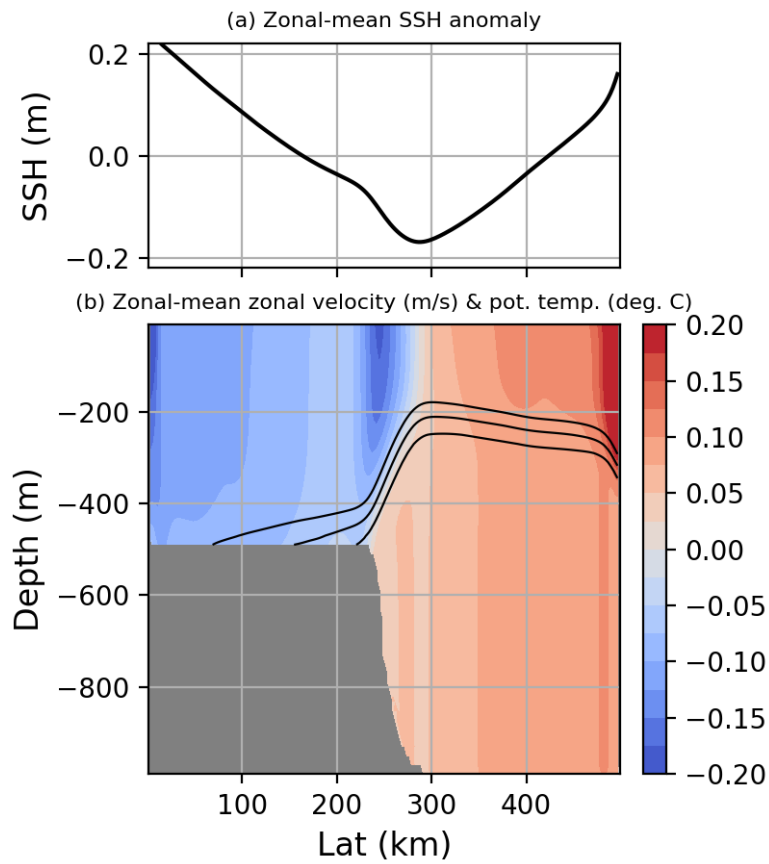


Figure 5: Outputs from the zonally uniform idealised model. (a) Zonal-mean SSH anomaly (versus latitude) averaged over the final year of a 30-year simulation. (b) Time-mean, zonal-mean zonal velocity (units m s^{-1}) versus latitude and depth. Positive (red) corresponds to eastward flow and negative (blue) corresponds to westward flow. In (b) the black lines represent the -0.5°C , 0°C and 0.5°C contours of θ , with colder contours nearer the surface.

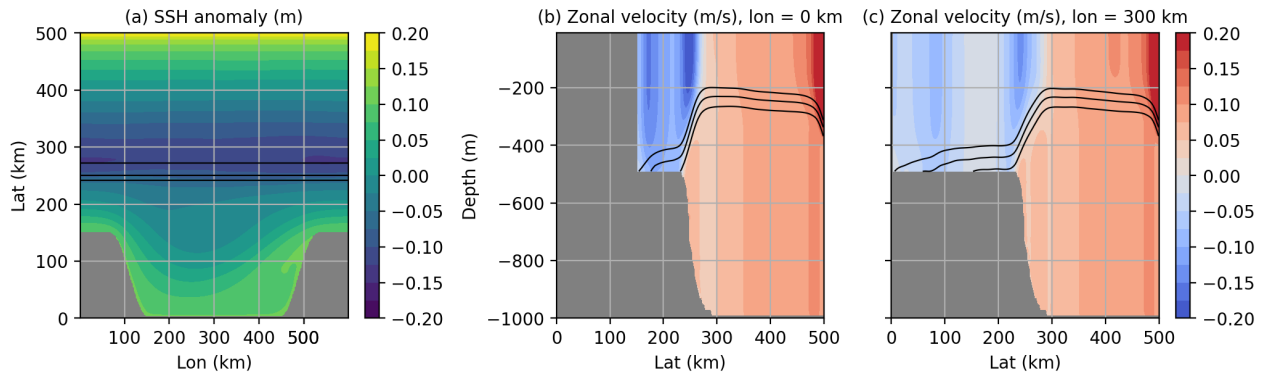


Figure 6: Outputs averaged over the final year of a 30-year simulation of the idealised model with a walled bay region on the shelf. (a) A plan view of the SSH anomaly. The three black lines are the -950 m, -750 m and -550 m contours of the bottom bathymetry. (b) A latitude-depth slice of the zonal velocity (units m s^{-1}) at a ‘walled’ longitude, $x = 0$ km. (c) A latitude-depth slice of the zonal velocity (units m s^{-1}) at a ‘bay’ longitude, $x = 300$ km. In panels (b) and (c) the black lines represent the -0.5°C , 0°C and 0.5°C contours of θ .

324 and vorticity balances cannot be attained in the same way as in the periodic case. There remains a narrow
 325 latitudinal range on-shelf which is periodic, but because this is connected to a walled area with the same f/h
 326 values, and because at some longitudes these walls are close to the continental slope, the dynamics in this
 327 latitudinal range differ to the previous case.

328 In figure 6a we show the SSH anomaly in the updated domain, averaged over the final year of the 30-year
 329 simulation. Figure 6b shows the zonal velocity u in the updated domain at a ‘walled’ longitude, $x = 0$ km.
 330 Figure 6c shows u at a ‘bay’ longitude, $x = 300$ km. As in the zonally uniform case, the flow is strongly
 331 barotropic at most locations. At the walled longitudes the wind-driven southward mass convergence at the
 332 coast maintains a SSH gradient with a relatively small latitudinal range of shelf over which baroclinic eddies
 333 can act to flatten the gradient. The result is a relatively fast barotropically unstable westward coastal current.
 334 After entering the bay the current broadens, as characterised by a less steep SSH gradient. Mass conservation
 335 can be used to explain the zonally varying speed of the westward current on the shelf. At the walled longitudes
 336 there is a relatively small latitude-depth open shelf area through which mass can be transported. At the bay
 337 longitudes, there is a relatively large area through which mass can be transported. Therefore, since two such
 338 longitudes must have the same zonal mass transport in steady state, the current must be faster at the walled
 339 longitudes and slower at the bay longitudes.

340 Figures 6b,c show that the flow response features a second westward current that is attached to the continen-
 341 tal slope, in addition to the coastal current. At the walled longitudes, the two currents run close to one another,
 342 while they have a broad separation at the bay longitudes. The two westward currents in this configuration of
 343 the idealised model can be interpreted as simple representations of the AACC and the ASC. While the AACC
 344 is present in the regional model and the real world, the ASC is not present in the regional model and is thought
 345 to have a weak signal in the real Amundsen Sea [Thompson et al., 2020]. The ASC has too strong a signal in
 346 this idealised model, in effect due to the ASF beneath; at these latitudes where the domain is zonally uniform
 347 and periodic, the strong SSH gradient and associated ASC are required in order to compensate for the ASF,
 348 so that the weak surface stresses can be balanced by weak bottom friction in the zonal momentum budget.

3.2.3 Adding the PITE trough and ridge

We now consider the addition of the PITE trough and ridge (at PITE and R in figure 2a) to the bathymetry of the idealised model. The geometries and locations of the trough and ridge are guided by their characteristics shown in figure 2: the ridge extends to the shelf break, has a minimum depth of 400 m, and is approximately 60 km wide. In the regional model the ridge is the westernmost feature amongst relatively shallow topography between the Bellingshausen Sea and the Amundsen Sea embayment. In the context of the idealised model we will discuss the role of the ridge in blocking deep inflow from the east; in the regional model this blocking is done by shallow topographic features over a greater longitudinal range, rather than just by the ridge.

Figure 7 shows the deep flow ($z = -450$ m) averaged over the final year of 30-year simulations for a selection of bottom bathymetries. For reference, figure 7a shows the deep flow for the case of no bottom bathymetry on the shelf, the same simulation as in figure 6. We opt to not show the surface flow for brevity, but this can be mostly inferred given that the flow is strongly barotropic away from the continental slope.

After adding the PITE trough (figure 7b), the deep westward current (and surface current, not shown) passes to the south of the PITE trough and meanders in its wake. The trough guides the ASC portion of the westward flow to the south and back to the north again. The overall result is a flow pattern that is not topologically distinct from the case without a trough. In this case, though, the AACC does not stick strictly to the coast in the east of the bay and instead meanders across the bay before reaching the western side of the bay.

In the case with just a ridge in the east (figure 7c) we observe a qualitatively different flow response. Deep inflow from the east is now blocked by the ridge, just as in the regional model. Since there is now blocking of potential vorticity contours in the zonal direction at all latitudes on the shelf, vorticity balance cannot be maintained by a periodic flow, unlike in the zonally uniform case. Instead, vorticity imparted at the surface by the cyclonic winds is extracted at the ocean floor by a deep cyclonic circulation and the associated bottom friction. This also means that unlike in the zonally uniform case, the (approximately) locally balanced zonal momentum budget does not exist. In short, by adding walls to the continental shelf the on-shelf dynamics have switched from being analogous to those of the Antarctic Circumpolar Current to those of a North Atlantic Gyre. The northern section of the deep circulation in the simulation with a ridge includes a strong eastward current that was previously absent. This deep current turns southwards when it encounters the ridge in the east as it is blocked by the f/h gradient of the ridge.

If the ridge were inverted to be a trough with f/h contours that intersect with the boundary, then we would attain a flow response similar to the case with just the PITE trough (results not shown for brevity). In this case, despite there being no periodic f/h contours on the shelf, deep flow still passes over this inverted ridge. This is because in our parameter regime the topographic form stresses associated with flow across the bathymetric contours of the trough can be balanced by nonlinear advection of westward momentum across the trough. Such a balance is achieved with westward flow that accelerates as it starts to cross the trough and decelerates as it approaches the flat section of bathymetry on the other side.

Lastly, compared to the case with just the ridge, inclusion of both the PITE trough and ridge leads to a cyclonic circulation which is shifted slightly to the west. This is simply because the PITE trough blocks the eastward current from travelling any further to the east and directs instead it to the south, as in the regional model. Also as in the regional model, we emphasise that the mean deep current does not flow in the depths of

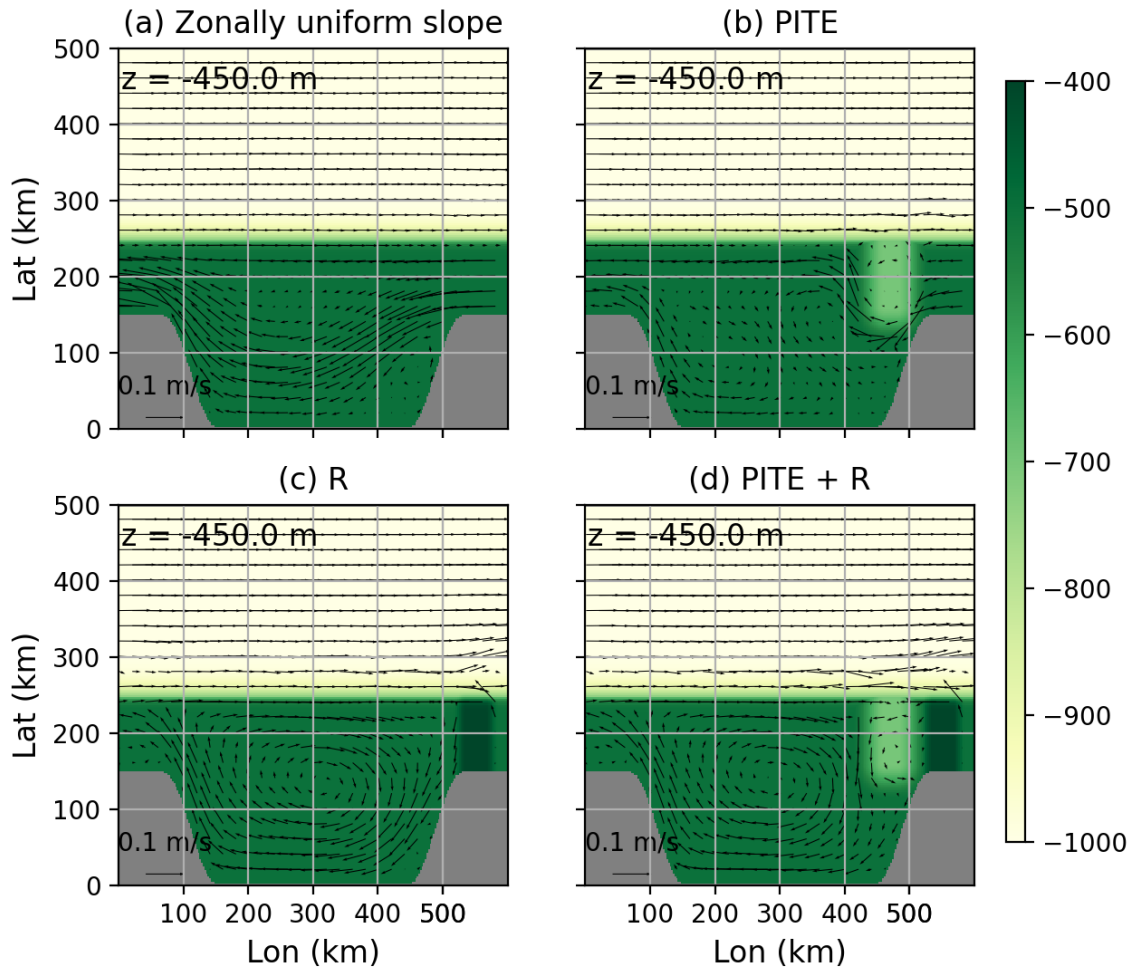


Figure 7: Vector plots of the deep flow ($z = -450$ m) averaged over the final year of 30-year simulations for a selection of bottom bathymetries in the idealised model. (a) Deep flow in the case of no bottom bathymetry, i.e., the same simulation as in figure 6. (b) Deep flow with a trough in the east. (c) Deep flow with a ridge in the east. (d) Deep flow with the PITE trough and ridge. In all panels colour represents the bottom bathymetry.

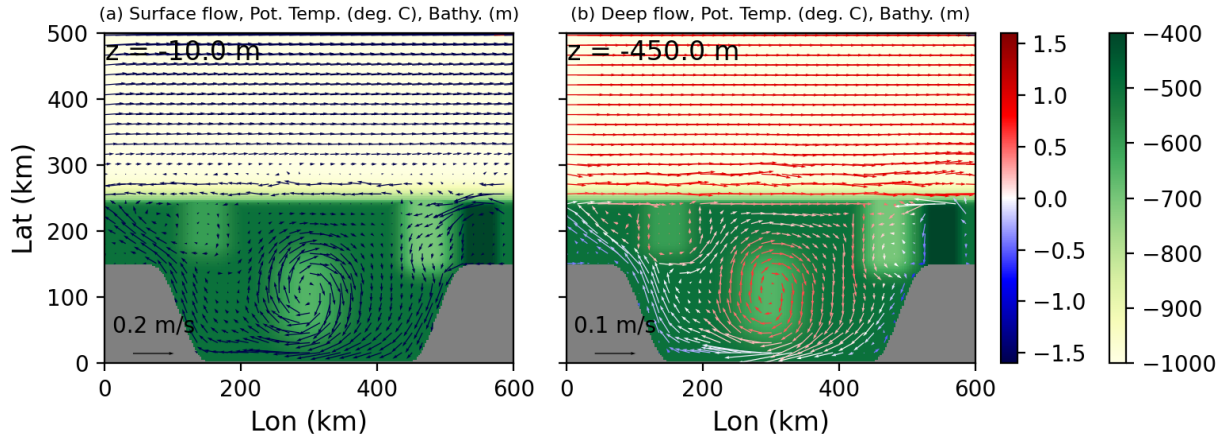


Figure 8: The flow response in the idealised model with the PITW trough, central basin, PITE trough and ridge. Shown are (a) the surface ($z = -10$ m) flow and (b) the deep ($z = -450$ m) flow. In both panels arrow colour represents the local potential temperature and background colour represents the bottom bathymetry. All data are averaged over the final year of a 30-year simulation.

389 the PITE trough.

390 These results suggest that by blocking deep inflow from the east, the ridge creates a deep cyclonic flow that
 391 spans the eastern Amundsen Sea embayment. Without the ridge, deep inflow from the east would counter any
 392 deep eastward current on the northern section of the continental shelf. That is, the ridge permits the presence
 393 of a deep cyclonic circulation on the shelf that has a strong eastward-flowing limb immediately to the south of
 394 the shelf break. Note, in the cases with the ridge the surface flow remains periodic since it can pass over the
 395 ridge, representing a significant deviation from the largely barotropic flow in cases without the ridge.

396 3.2.4 Adding the central basin and PITW trough

397 We now add a central basin and PITW trough to the idealised bathymetry – for reference, in the regional model’s
 398 realistic bathymetry these features are denoted as C and PITW in figure 2a. As before our representations of
 399 these features are highly idealised but serve to reproduce the qualitative influence of the corresponding features
 400 in the regional model.

401 Figure 8 shows the surface (a, $z = -10$ m) and deep (b, $z = -450$ m) flow and potential temperature. Also
 402 shown is the the updated bathymetry. As before, data are averaged over the final year of a 30-year simulation.
 403 Like in the regional model, our idealised representation of the central basin doesn’t extend all the way to the
 404 shelf break, and therefore doesn’t inhibit cyclonic flow to its north. The PITW trough is shallower than the
 405 PITE trough. Details that we are not including in this bathymetric configuration, with simplicity in mind, are
 406 the f/h contours that connect the PITW trough to the central basin and PITE trough. However, we do not
 407 need to include this detail of the bathymetry to realise the deep eastward current on the shelf.

408 With the new bathymetry, the surface flow consists of a cold and fresh coastal current which enters the
 409 domain from the east, passes to the south of the central basin and then leaves the domain in the west. This
 410 surface current is similar to the current in the simulations without the central basin (not shown), the main
 411 difference being the central basin causing the current to cross the bay further to the south. When it enters the

412 bay from the east, the surface flow has a tendency to pass to the north of the ridge, rather than directly over it.
413 If we included near-surface stratification (in salinity) in the idealised model, as is present in the regional model,
414 this would permit the surface current to pass directly over the ridge, as it does in the regional model. The
415 surface flow features a notable cyclonic circulation, in particular in the central basin, which is stronger than in
416 the regional model. This circulation is strong in the idealised model because of a lack of vertical stratification
417 and the abundance of closed f/h contours in our simple bathymetry which are not present in the regional
418 model.

419 At depth the main feature of the flow is the cyclonic circulation. As before, the northern limb of this
420 circulation is the deep eastward current which turns south when it becomes blocked by the PITE trough. Like
421 in the regional model, this southward flow proceeds from the western edge of the PITE trough to the eastern
422 edge of the central basin. To the east of the central basin is where the deep flow is warmest, due to the
423 southward advection of warm waters that have recently broken across the shelf – we discuss this heat transport
424 more in the next section.

425 The deep current continues on a cyclonic trajectory about the central basin. After passing to the south
426 and west of the central basin, the majority of this flow leaves the bay to the west. The remainder of the flow
427 remains in the bay and forms a closed cyclonic circulation about the central basin. A closed deep circulation
428 such as in this idealised model is commonly observed at specific instances in time in the regional model, but is
429 not consistent enough to have a marked signal in the mean flow (figure 2b). Most of the deep flow that has left
430 the bay to the west in the idealised model is forced to turn and reenter the bay to the west of the PITW trough.
431 The small remainder continues flowing west and passes to the north of the ridge; this latter flow feature is not
432 present in the regional model.

433 The PITW trough plays a smaller role in the idealised model compared to in the regional model. In both
434 models an eastward current flowing along the continental slope and shelf break turns into the PITW trough.
435 This current overshoots the western rim of the trough and crosses f/h contours in a manner similar to the
436 simulations of Assmann et al. [2013]. While in the regional model these waters tend to remain on the shelf –
437 aided by f/h contours between the PITW trough and the central basin – this is less common in the idealised
438 model given its simpler bathymetry. Instead, in the idealised model there is only a weak mean flow of waters
439 that escape the confines of the PITW trough (mainly near its south-eastern corner) to reach the flat sections
440 of the shelf.

441 3.3 Heat transport

442 3.3.1 Heat fluxes

443 In this section we discuss the transport of heat onto the continental shelf and the role of bathymetric features in
444 the idealised model. We first consider the area-integrated cross-shelf heat fluxes (through the latitude $y = 240$
445 km). We define the heat flux as $\rho_0 C_p v(\theta - \theta_0)$, where v is the meridional velocity, $\rho_0 = 1030 \text{ kg m}^{-3}$ is the
446 reference density and $C_p = 3974.0 \text{ J kg}^{-1} \text{ C}^{-1}$ is the heat capacity. For the reference temperature we use
447 $\theta_0 = -1.8^\circ\text{C}$, the value used for the uniform initial condition. The local freezing temperature could have been
448 used instead, from which we would make the same conclusions.

449 In figure 9 we show time series of the monthly area-integrated cross-shelf heat fluxes. In each case we show
450 the total cross-shelf heat flux, the heat flux across longitudes where the shelf topography is zonally uniform,

451 and the heat flux across longitudes where there is a trough or ridge. All total cross-shelf heat fluxes are negative
452 (southwards) and can be so in an equilibrated state because of the cooling by the relaxation at the southern
453 boundary. The time series are largely insensitive to adjustments of a few grid points to the limits of the
454 longitudinal sections.

455 Figure 9a is for the bathymetry with just the PITE trough. In this case the heat fluxes at the PITE trough
456 and the uniform longitudes are strongly anti-correlated, with the two time series summing to a small negative
457 value. This behaviour is due to an along-continental slope westward current that meanders when it encounters
458 the trough. The net on-shelf heat flux (black line) is balanced by heat removal by the relaxation at the southern
459 boundary. This net transfer of heat onto the shelf is only marginally greater than in the uniform shelf case (see
460 next section for evidence of this).

461 Figure 9b is for the bathymetry with the PITE trough and ridge. This simulation has net heat fluxes across
462 the shelf break approximately twice as large as the simulation with just the PITE trough. Almost all of this
463 heat is fluxed onto the shelf at the longitudes of the PITE trough and ridge, and most of this heat fluxed onto
464 the shelf is fluxed off the shelf at uniform longitudes. Figure 9c is for the bathymetry with the two troughs, the
465 ridge and the central basin. Results are similar to those in figure 9b, the main difference being the additional
466 source of heat provided by fluxes at the PITW trough. Compared to the previous case, this additional on-shelf
467 heat flux is compensated for by greater off-shelf heat fluxes at the uniform longitudes. The result is a net
468 on-shelf heat flux approximately the same as in the PITE trough and ridge case.

469 These time series illustrate the role that along-shelf topographic variability plays in enhancing cross-shelf
470 break heat fluxes. In the case of a zonally uniform shelf break, the only physical processes by which heat can be
471 fluxed onto the shelf are baroclinic instability and bottom Ekman transport. The latter is negligibly small in
472 our simulations and the former mechanism is suppressed by the bottom gradient associated with the continental
473 slope. By adding troughs and/or a ridge to to the uniform shelf break additional mechanisms can now induce
474 southward flow and heat fluxes across the shelf break.

475 Small-scale topographic variability at the troughs/ridges on the shelf break causes breaks in geostrophy
476 and induce southward flow across the shelf break. That is, the small-scale topographic variability reduces the
477 lengthscales (L) of the local flow regime, increases the Rossby number ($Ro = U/fL$, with velocity scale U)
478 and hence causes the flow to deviate from geostrophic balance [Allen and de Madron, 2009, Allen and Hickey,
479 2010, Zhang and Lentz, 2018]. It is precisely the sharp turns in the along-shelf f/h contours at the trough
480 mouths/ridge (a feature of both regional model and idealised model bathymetries) that reduce the local flow
481 lengthscales. The necessary lengthscale is the radius of curvature [Klinck and Dinniman, 2010, Allen and
482 Hickey, 2010] of the trough mouths/ridge, which is on the order of a few km. We may compare this with the
483 uniform shelf lengthscale of 600 km, suggesting an increase in the Rossby number by two orders of magnitude
484 for flows at the trough mouths. For reference, the local baroclinic deformation radius is approximately 10 km.

485 With the deviation from geostrophic balance at along-shelf topographic features, the southward pressure
486 gradient force and northward temperature gradient both associated with the ASF induce southward heat fluxes
487 across the shelf break, i.e., across f/h contours. Precisely where the fluxes have a tendency to cross the shelf
488 break is different for each topographic configuration and for each trough/ridge. The spatial anomalies in the
489 meridional velocity are small in spatial scale (a few km wide), but since they are excited over topographic
490 variability they have non-zero time mean.

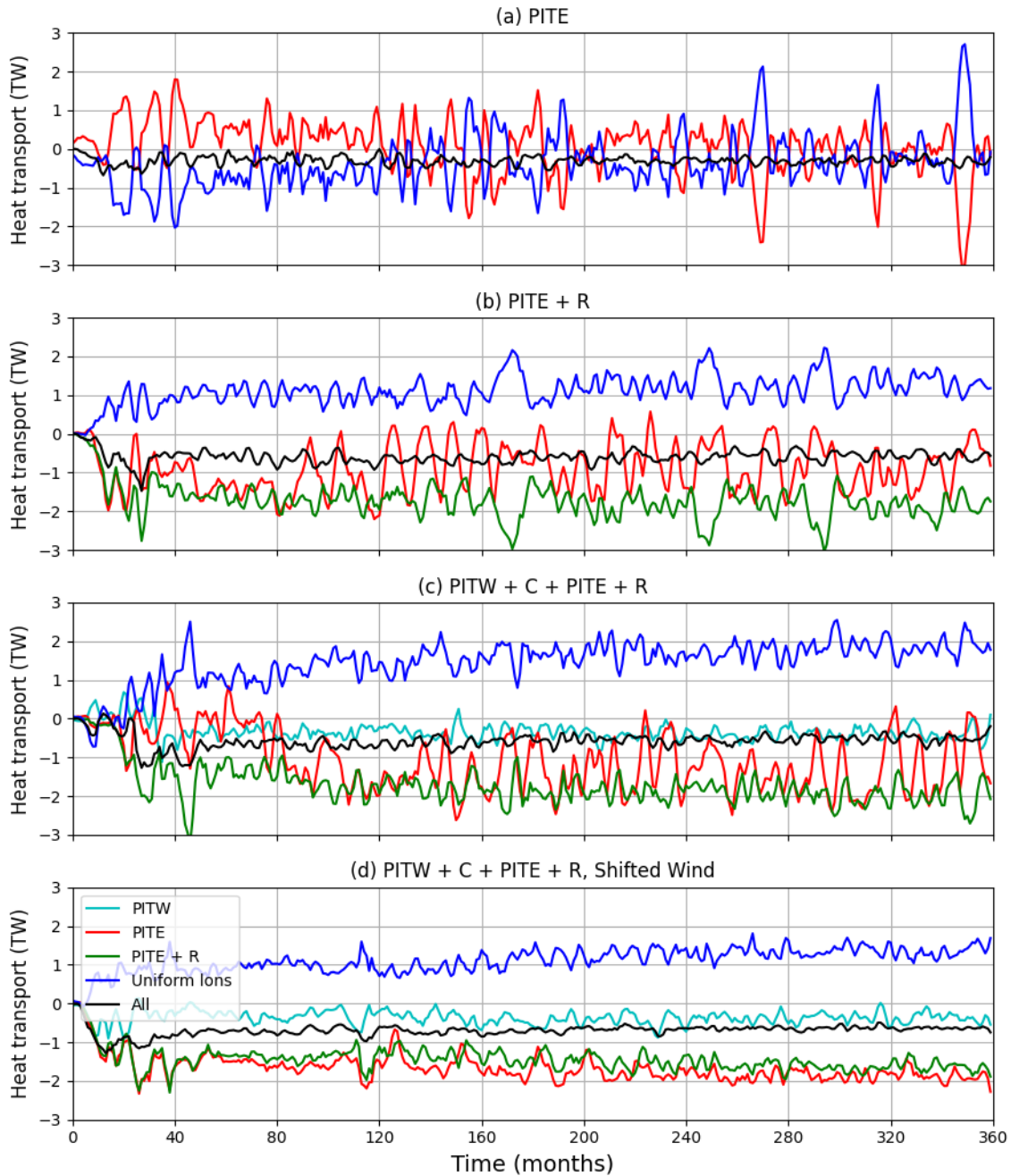


Figure 9: Time series of integrated meridional heat fluxes (units TW) across the shelf break in different longitudinal sections. The local heat flux is $\rho_0 C_p v(\theta - \theta_0)$, where v is the meridional velocity and $\theta_0 = -1.8^\circ\text{C}$ is the reference potential temperature. Negative values denote a heat flux onto the shelf. Results are for simulations with bathymetries with: (a) PITE trough only; (b) PITE trough and ridge; (c) both troughs, central basin and ridge. Panel (d) is the same as for panel (c) but with the wind profile shifted southwards by 40 km. We present the heat flux across all longitudes (black), across just the uniform longitudes, i.e., where there are no troughs or ridge (blue) and across longitudes with a trough or ridge (see legend for details). The presented time series use a 3-monthly running average to aid interpretability.

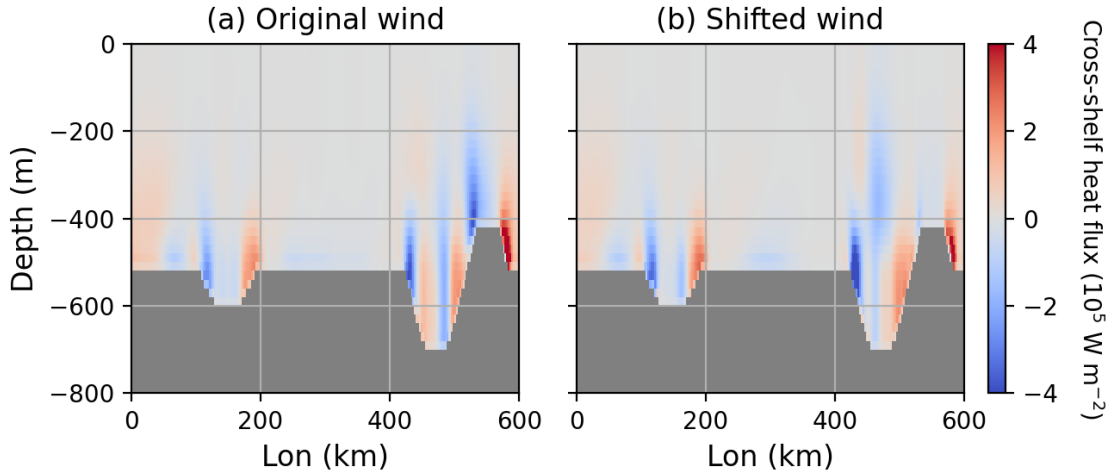


Figure 10: Latitude-depth slices of the cross-shelf heat flux (through $y = 240$ km), namely $\rho_0 C_p v(\theta - \theta_0)$. These are for simulations with (a) the original wind and (b) the wind shifted southwards 40 km. Both simulations use the idealised bathymetry with the two troughs, the ridge and the central basin. Negative values denote a southward flux. Data area averaged over the final year of 30-year simulations.

491 When the local Rossby number increases, the momentum tendency and momentum advection terms become
 492 more important in the meridional momentum budget. This increased role of momentum advection in cross-shelf
 493 exchange is also described by Dinniman et al. [2003] and Dinniman and Klinck [2004]. In the vorticity budget,
 494 this flow across f/h contours is associated with a balance between vortex stretching and vorticity advection.

495 The cases with the ridge have net on-shelf heat fluxes approximately twice as large as the cases without the
 496 ridge. The inclusion of the ridge precludes the existence of a strong current flowing along the shelf break that
 497 exists in the cases without the ridge. In these cases without the ridge the along-shelf current acts as a transport
 498 barrier [Ferrari and Nikurashin, 2010] and suppresses heat fluxes onto the shelf. In contrast, simulations with
 499 a ridge instead feature a deep cyclonic circulation on the shelf, which does not act as a transport barrier along
 500 the entire length of the shelf break. Another important role of the cyclonic circulation is that it transports heat
 501 fluxed onto the shelf towards the south.

502 Figure 10a shows a longitude-depth slice of the cross-shelf meridional heat flux for the bathymetry with
 503 the two troughs, the ridge and the central basin. When the eastward undercurrent reaches either trough it
 504 turns into the trough on its western side and flows out of the trough on its eastern side. An additional heat
 505 flux dipole in the centre of the PITE trough is due to a small-scale cyclonic circulation at the trough mouth.
 506 In their model with realistic bathymetry, Kimura et al. [2017] diagnosed strongest heat fluxes across the shelf
 507 break at the eastern sides of the troughs, as opposed to the western sides as in our idealised model. The realistic
 508 models of Assmann et al. [2013] and Dotto et al. [2020] show the same phenomena. This difference between
 509 our idealised model and the more realistic models is due inertial overshoots of the eastward undercurrent as
 510 it reaches each trough being relatively weak in the idealised model. Lastly, we note the relatively strong heat
 511 fluxes either side of ridge, caused by some of the westward outflow from the bay region passing to the north
 512 of the ridge. In doing this, this flow moves northwards upstream of the ridge, crossing f/h contours, before
 513 returning southwards downstream of the ridge.

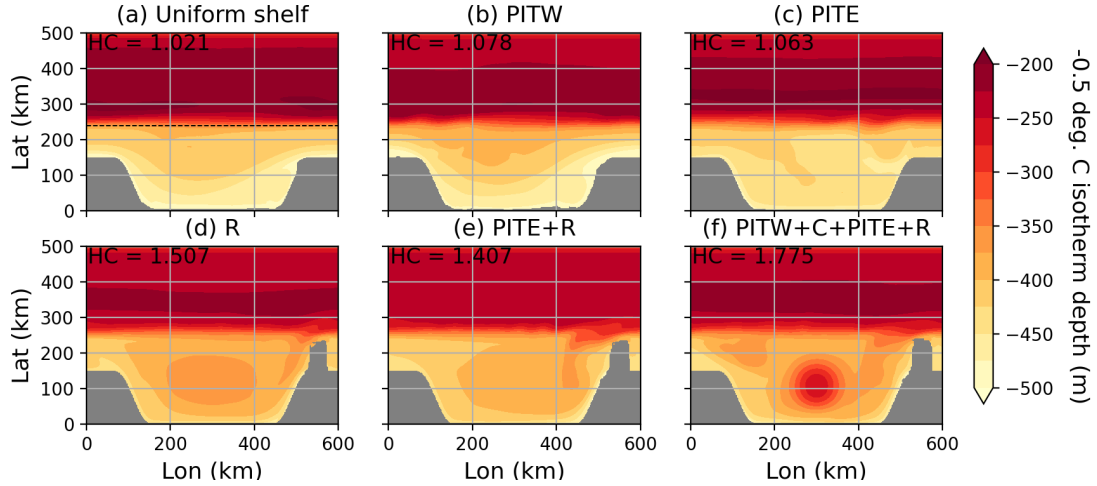


Figure 11: The $\theta = -0.5^\circ\text{C}$ isotherm depth for a selection of simulations with different bathymetries. Data is for the isotherm averaged over the final year of the respective 30-year simulations. The six cases are: (a) zonally uniform shelf, (b) shelf with PITW trough, (c) shelf with PITE trough, (d) shelf with ridge, (e) shelf with PITE trough and ridge, and (f) shelf with PITW, PITE troughs, the central basin and the ridge. Grey masked regions are where the $\theta = -0.5^\circ\text{C}$ isotherm does not exist. In each panel we also provide the on-shelf heat content, denoted HC, which is given in units 10^{20} J. The northern boundary of the shelf region is set at a latitude of 240 km, as depicted by the dashed line in (a).

514 3.3.2 Heat content

515 As a measure of the on-shelf heat distribution we now use the depth of the $\theta = -0.5^\circ\text{C}$ isotherm. We will also
 516 use the on-shelf heat content, denoted HC and defined as

$$\text{HC} = \int_{\Omega} \rho_0 C_p (\theta - \theta_0) d\Omega. \quad (1)$$

517 As before, the reference temperature is $\theta_0 = -1.8^\circ\text{C}$. With this choice the only source for on-shelf heat content is
 518 from waters fluxed across the shelf break; the initial conditions have an on-shelf heat content of zero. Integration
 519 is implemented over the volume Ω , defined to contain the entire zonal range and to span from the southern
 520 boundary to the shelf break at $y = 240$ km. Depth integration is applied over the entire water column but
 521 the PITW and PITE troughs at depths greater 500 m are omitted (the central basin is not omitted). We
 522 do not consider warm waters within the depths of the troughs as being on the shelf as these waters require
 523 an additional upwelling mechanism before they may reach the upper, flat section of the shelf. Further, these
 524 warm waters can be contained within large-scale geostrophic currents that flow out of the depths of the troughs
 525 shortly after flowing in.

526 The $\theta = -0.5^\circ\text{C}$ isotherm depth (averaged over the final year of 30-year simulations) is shown in figure 11
 527 for a selection of bathymetries. Also provided in each panel is the on-shelf heat content, HC. The case of the
 528 uniform continental slope (figure 11a) has the lowest on-shelf heat content (1.021×10^{20} J) due to a relatively
 529 stable ASF. The ASF remains stable because the continental slope suppresses baroclinic instability, and with
 530 no along-shelf break topographic variability there is a lack of mechanisms to induce meridional exchange. The
 531 simulations with the western (figure 11b) and eastern (figure 11c) troughs have marginally greater on-shelf
 532 heat contents of 1.078×10^{20} J and 1.063×10^{20} J, respectively. Although in these simulations the troughs can

533 induce cross-shelf exchange of heat, the on-shelf heat content is only marginally greater than in the zonally
534 uniform case because of the along-shelf break flow that acts as a transport barrier [Ferrari and Nikurashin,
535 2010], inhibiting fluxes of heat onto the shelf.

536 The simulations with the ridge have greater on-shelf heat contents compared to the simulations without a
537 ridge. The heat content values are 1.507×10^{20} J for the case with just the ridge (figure 11d), 1.407×10^{20} J
538 for the case with the PITE trough and ridge (figure 11e), and 1.775×10^{20} J for the case with all topographic
539 features we consider (figure 11f). These greater heat contents are due to simulations with a ridge featuring a
540 deep cyclonic circulation instead of a strong along-shelf break flow. Unlike the along-shelf break current, the
541 deep cyclonic circulation does not act as a transport barrier along the length of the shelf break.

542 The deep cyclonic circulation entrains heat fluxed across the shelf break and transports it southwards. The
543 southward transport in the cyclonic circulation is evidenced by the warm tongue in the eastern side of the bay,
544 a feature which also exists in the regional model (figure 3a). Much of the heat fluxed onto the shelf is stored
545 in a heat ‘dome’ in the centre of the shelf. This heat dome is most pronounced in the simulation with the
546 central basin (figure 11f). This is the case because the bathymetry gradient around the edges of the central
547 basin permit a steeper stable lateral isotherm gradient because of its suppression of baroclinic instability. The
548 consequence is that we diagnose the greatest on-shelf heat content in the case with the central basin; that
549 more of the heat fluxed onto the continental shelf is stored in the heat dome means less heat is removed at
550 the southern boundary by the relaxation. A similar heat dome over the deepest part of the central basin is
551 diagnosed in the regional model (figure 3a), and in the model results of Webber et al. [2019].

552 **3.4 A simulation with meridionally shifted winds**

553 So far in this study we have considered a single wind profile. It is known, though, that the winds in the
554 Amundsen Sea region are highly variable and are changing on climatic timescales. To understand the effects of
555 such changes is of great importance. The Southern Annular Mode (SAM), which reflects the position/intensity
556 of surface westerly winds around Antarctica, is an important descriptor of the winds in the Amundsen Sea
557 region. Recent decades have seen a positive SAM trend, i.e., a strengthening and southward shift of the
558 Southern Hemisphere westerly winds, which is an expected response of the Southern Hemisphere climate to
559 anthropogenic forcings [Arblaster and Meehl, 2006, Gillett et al., 2013, Goyal et al., 2021]. Studies have
560 simulated the response to such a wind trend in the Amundsen Sea region [Donat-Magnin et al., 2017] and
561 around the entirety of Antarctica [Spence et al., 2014] in realistic climate simulations. These studies show that
562 the responses to possible future wind scenarios are complex. However, a consistent prediction is that under
563 these wind changes deep coastal waters are warmed, in turn leading to increased basal melting of the ice shelves.

564 Motivated by past studies and the recent SAM trend, we will use a wind profile obtained by translating the
565 original profile south by 40 km (figure 4a, dotted curve). This represents a great simplification of actual predicted
566 changes to the winds. For example, in the new profile the winds on the continental shelf are changed, but recent
567 work [Holland et al., 2022] shows that only winds over the deep ocean have changed due to anthropogenic effects
568 in past decades, as is also the case in future emission scenarios. Given the great simplification in our choice
569 of second wind profile, this section will only be a very preliminary investigation into the effects of future
570 wind changes. However, the aim is that this will serve to motivate and inform more comprehensive future
571 investigations.

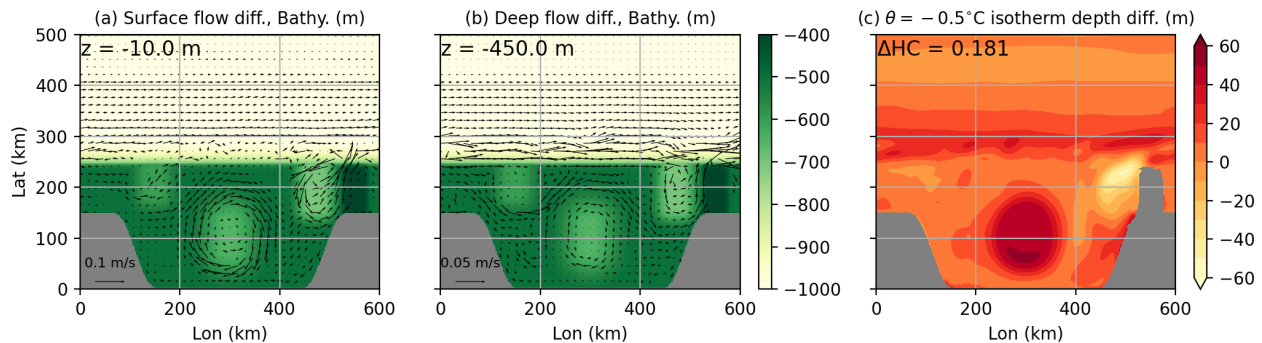


Figure 12: The flow in the simulation with meridionally shifted winds minus the flow from the simulation with the original winds. We plot results (a) near the surface ($z = -10$ m) and (b) at depth ($z = -450$ m). (c) The difference in the $\theta = -0.5^\circ\text{C}$ isotherm depth for the same two simulations. Positive values correspond a shallower isotherm, i.e., more heat, for the case of shifted winds. For all panels, data are averaged over the last year of 30-year simulations.

572 In figure 12 we plot the difference between the flow response in this new simulation and the flow response
 573 from the case with the original winds. These are for the surface layer (a, $z = -10$ m) and at depth (b, $z = -450$
 574 m). Shifting the winds southward leads to a weaker westward inflow and marginally stronger on-shelf cyclonic
 575 circulation in the surface flow. A similar acceleration of the cyclonic circulation occurs at depth, with the
 576 eastward-flowing limb being affected most. Previous studies have discussed the phenomena of a barotropic
 577 acceleration of eastward undercurrent and on-shelf flow as a result of southward shifts in the wind profile over
 578 the Amundsen Sea shelf break [Thoma et al., 2008, Kimura et al., 2017, Holland et al., 2019, Bett et al., 2020,
 579 Dotto et al., 2020]. This eastward acceleration is part of a broader cyclonic acceleration, which itself is due to
 580 the winds being more cyclonic over the continental shelf after being shifted.

581 In figure 12c we show the difference between the $\theta = -0.5^\circ\text{C}$ isotherm depths in the shifted-wind and original-
 582 wind simulations. Positive values denote a shallower isotherm (i.e., more heat on shelf) in the simulation with
 583 shifted winds. The on-shelf heat content averaged over the final year of the simulation is 1.956×10^{20} J, greater
 584 than the heat content of 1.775×10^{20} J in the case of the original winds. The majority of this additional heat
 585 in the case of shifted winds is contained within the lateral confines of the central basin.

586 Figure 9d shows time series of the cross-shelf heat fluxes for the case of southward shifted winds, which
 587 can be compared with figure 9c which is for the original winds. Aggregated over all longitudes, the southward
 588 cross-shelf heat flux is marginally greater after shifting the winds, consistent with heat content values. This is
 589 the case despite there being slightly less heat fluxed across the shelf near the troughs and ridge for the shifted
 590 wind simulation. The greater net cross-shelf heat flux and on-shelf heat content is instead a consequence of
 591 weaker off-shelf fluxes at uniform longitudes, this in turn possibly due to weaker coastal downwelling in the
 592 south. The temporal variability of the heat fluxes is notably reduced in the case of the shifted winds because
 593 the variability of the currents flowing near the shelf break has reduced.

594 Figure 10b shows a longitude-depth slice of the cross-shelf meridional heat flux for this case with the shifted
 595 wind. These cross-shelf heat fluxes are very similar to those in the case of the original wind profile. The main
 596 differences are: (1) a slight strengthening of the shoreward heat flux at the western sides of the troughs, (2) a
 597 weakening of the cyclonic circulation and associated heat fluxes in the centre of the PITE trough, and (3) a

598 significant weakening of the heat fluxes either side of the ridge.

599 Here we have made some simple conclusions, but the response to meridionally shifted winds is complex and
600 the result of compensating changes in the flow response. The wind changes that we have considered here are
601 much simpler than the real-world wind changes. The real-world changes are extremely complex, with natural
602 and anthropogenic trends having different spatial and seasonal patterns. A whole study will be required to
603 conduct a full examination of wind sensitivities.

604 4 Discussion and Conclusions

605 In this study we have developed an idealised model of the circulation in the Amundsen Sea, West Antarctica,
606 with a focus on the eastern Amundsen Sea region. This region is of particular interest given that ice shelves in
607 the area, such as Pine Island Glacier and Thwaites Glacier, have concerningly large mass loss rates due to rapid
608 basal melting [Pritchard et al., 2012, Mouginot et al., 2014, Rignot et al., 2014, Joughin et al., 2014]. One of
609 the main reasons for the high melt rates is the great access that warm Circumpolar Deep Water (CDW) has to
610 the continental shelf and the bases of the floating ice shelves [Jacobs et al., 1996, Walker et al., 2007, Dutrieux
611 et al., 2014, Heywood et al., 2016]. This is in contrast to many other sections around Antarctica where a strong
612 Antarctic Slope Front (ASF) separates off-shelf CDW from cooler and fresher shelf waters [Thompson et al.,
613 2018].

614 The winds over the Amundsen Sea are thought to be a key factor in controlling the access of warm waters
615 to the ice shelves. A southward shift and intensification of the polar westerlies of recent decades has been
616 linked to warming of deep coastal waters [Spence et al., 2014, Donat-Magnin et al., 2017]. While a south-
617 ward shift/eastward acceleration of the Southern Hemisphere westerlies is in general an expected response to
618 anthropogenic forcings [Arblaster and Meehl, 2006, Gillett et al., 2013, Goyal et al., 2021], it is not known
619 if this trend will continue in the coming decades. Holland et al. [2019] and Naughten et al. [2022] have also
620 attributed warming of the Amundsen Sea embayment to an anthropogenically forced eastward wind trend at
621 the shelf break. However, recent work [Holland et al., 2022] suggests that anthropogenic effects have had and
622 will continue to have little effect on the winds over the continental shelf, but are responsible for an acceleration
623 of the polar westerlies that flow over the deep ocean.

624 To confidently predict what effects future wind variations will have in the region it is first necessary to
625 attain a comprehensive understanding of the present-day dynamics. Realistic regional models are useful for
626 this task, but due to their associated computational demands it is often unfeasible for such models to be run
627 many times. It is also the case that interpreting the outputs of these models can be overly challenging. In
628 contrast, the relative simplicity of models with idealised forcing and geometries means we can more easily and
629 confidently interpret the involved physics. Such models are additionally useful because they can be run a large
630 number of times, enabling a broad exploration of parameters and configurations. In this study we develop a
631 sequence of idealised models of the dynamics in the eastern Amundsen Sea, with the aim to reproduce important
632 features as simulated by a regional model. By doing this we can make clear conclusions about the roles of winds
633 and bathymetry in shaping the circulation in the region, thus enabling more confident predictions of future
634 changes to the region. These results also help to guide future realistic modelling studies and possibly fieldwork
635 campaigns.

636 With the idealised models we concluded that the deep eastward current on the continental shelf – which

637 is part of a broader cyclonic circulation – exists because of sufficient blocking of deep inflow from the east by
638 a seabed ridge. In this case the vorticity budget is balanced by a deep cyclonic circulation: the surface stress
639 curl is opposed by the bottom stress curl, averaged over the whole shelf. The flow is particularly baroclinic
640 along the shelf break and continental slope, where the ASF causes deeper waters to more eastward-flowing than
641 waters above.

642 The idealised model results also suggest that without the deep current and the associated cyclonic circulation,
643 the shelf would be much cooler. This is because the circulation does not block cross-shelf heat fluxes, can entrain
644 heat fluxed across the shelf break, and can transport heat southwards. The circulating gyre stores heat on the
645 shelf in a heat dome, even in simulations without the central basin. With no blocking of the deep inflow from
646 the east, a different deep flow would exist, one which simply enters the eastern Amundsen Sea from east and
647 exits in the west. This current would have a tendency to remain close to the shelf break and inhibit cross-shelf
648 fluxes by acting as a transport barrier [Ferrari and Nikurashin, 2010].

649 Our results elucidate the role of topographic variability along the continental slope (e.g., troughs and ridges)
650 in enabling cross-shelf heat fluxes. Such topographic variability on sufficiently small scales will induce breaks
651 from geostrophy [Allen and de Madron, 2009, Allen and Hickey, 2010, Zhang and Lentz, 2018] and increase
652 cross-shelf flow. This is manifested as breakages in the ASF, within which the southward pressure gradient and
653 northward temperature gradient lead to a southward heat flux across the shelf break. Since the breaks from
654 geostrophic balance are caused by topographic variability, these heat fluxes are persistently excited in the same
655 locations in a given simulation.

656 The idealised model includes weak relaxation of θ and S towards a cold and fresh state at the southern
657 boundary. We repeated these simulations without this southern relaxation (results not shown) and find that
658 in steady state the continental shelf is warmer than is realistic. The flow fields are qualitatively similar to the
659 case with the southern relaxation switched on. That a realistic heat distribution is not observed in the model
660 equilibrium without the southern relaxation highlights the important role that other physical mechanisms play
661 in maintaining the quasi-mean on-shelf heat content in the regional model and real world. For example, Bett
662 et al. [2020] showed that ice shelf melt and sea ice melt/formation provide θ and S sources/sinks that are
663 important for maintaining the on-shelf heat distribution. Another mechanism is simple advection out of the
664 eastern Amundsen Sea by the mean currents, a process not realistically represented in the periodic idealised
665 model. Lastly, in the idealised model we imposed steady winds, while in reality the winds in the region are
666 highly variable, oscillating about a quasi-mean state. The nonlinearity of the dynamics means oscillatory winds
667 could lead to different flow patterns and cross-shelf fluxes than steady winds. Given the above points, the
668 priorities of future research will be deeper consideration of the buoyancy budget and the role of wind variability
669 in the Amundsen Sea region.

670 Acknowledgements

671 This research was funded by the NERC project “Drivers of Oceanic Change in the Amundsen Sea”, NE/T012803/1.

672 Data Availability Statement

673 The data and codes used in this study are in the process of being uploaded to trusted public data storage sites.

674 References

- 675 S. E. Allen and X. Durrieu de Madron. A review of the role of submarine canyons in deep-ocean exchange with
676 the shelf. *Ocean Science*, 5(4):607–620, dec 2009. doi: 10.5194/os-5-607-2009.
- 677 S. E. Allen and B. M. Hickey. Dynamics of advection-driven upwelling over a shelf break submarine canyon.
678 *Journal of Geophysical Research*, 115(C8), aug 2010. doi: 10.1029/2009jc005731.
- 679 Julie M. Arblaster and Gerald A. Meehl. Contributions of external forcings to southern annular mode trends.
680 *Journal of Climate*, 19(12):2896–2905, jun 2006. doi: 10.1175/jcli3774.1.
- 681 L. Arneborg, A. K. Wåhlin, G. Björk, B. Liljebladh, and A. H. Orsi. Persistent inflow of warm water onto the
682 central amundsen shelf. *Nature Geoscience*, 5(12):876–880, nov 2012. doi: 10.1038/ngeo1644.
- 683 K. M. Assmann, A. Jenkins, D. R. Shoosmith, D. P. Walker, S. S. Jacobs, and K. W. Nicholls. Variability
684 of circumpolar deep water transport onto the amundsen sea continental shelf through a shelf break trough.
685 *Journal of Geophysical Research: Oceans*, 118(12):6603–6620, dec 2013. doi: 10.1002/2013jc008871.
- 686 David T. Bett, Paul R. Holland, Alberto C. Naveira Garabato, Adrian Jenkins, Pierre Dutrieux, Satoshi Kimura,
687 and Andrew Fleming. The impact of the amundsen sea freshwater balance on ocean melting of the west
688 antarctic ice sheet. *Journal of Geophysical Research: Oceans*, 125(9), sep 2020. doi: 10.1029/2020jc016305.
- 689 Cédric P. Chavanne, Karen J. Heywood, Keith W. Nicholls, and Ilker Fer. Observations of the antarctic slope
690 undercurrent in the southeastern weddell sea. *Geophysical Research Letters*, 37(13):n/a–n/a, jul 2010. doi:
691 10.1029/2010gl043603.
- 692 Changheng Chen and Igor Kamenkovich. Effects of topography on baroclinic instability. *Journal of Physical*
693 *Oceanography*, 43(4):790–804, apr 2013. doi: 10.1175/jpo-d-12-0145.1.
- 694 Shih-Nan Chen, Chiou-Jiu Chen, and James A. Lerczak. On baroclinic instability over continental shelves:
695 Testing the utility of eady-type models. *Journal of Physical Oceanography*, 50(1):3–33, jan 2020. doi:
696 10.1175/jpo-d-19-0175.1.
- 697 Michael S. Dinniman and John M. Klinck. A model study of circulation and cross-shelf exchange on the
698 west antarctic peninsula continental shelf,. *Deep Sea Research Part II: Topical Studies in Oceanography*, 51
699 (17–19):2003–2022, 2004.
- 700 Michael S. Dinniman, John M. Klinck, and Walker O. Smith. Cross-shelf exchange in a model of the ross sea
701 circulation and biogeochemistry. *Deep Sea Research Part II: Topical Studies in Oceanography*, 50(22–26):
702 3103–3120, 2003.
- 703 Marion Donat-Magnin, Nicolas C. Jourdain, Paul Spence, Julien Le Sommer, Hubert Gallée, and Gaël Durand.
704 Ice-shelf melt response to changing winds and glacier dynamics in the amundsen sea sector, antarctica.
705 *Journal of Geophysical Research: Oceans*, 122(12):10206–10224, dec 2017. doi: 10.1002/2017jc013059.
- 706 Jun Dong, Kevin Speer, and Loic Jullion. The antarctic slope current near 30°e. *Journal of Geophysical*
707 *Research: Oceans*, 121(2):1051–1062, feb 2016. doi: 10.1002/2015jc011099.

708 B. Dorschel, L. Hehemann, S. Viquerat, F. Warnke, S. Dreutter, et al. The international bathymetric chart of
709 the southern ocean version 2. *Scientific Data*, 9(1), jun 2022. doi: 10.1038/s41597-022-01366-7.

710 Tiago S. Dotto, Alberto C. Naveira Garabato, Sheldon Bacon, Paul R. Holland, Satoshi Kimura, Yvonne L.
711 Firing, Michel Tsamados, Anna K. Wåhlin, and Adrian Jenkins. Wind-driven processes controlling oceanic
712 heat delivery to the amundsen sea, antarctica. *Journal of Physical Oceanography*, 49(11):2829–2849, nov
713 2019. doi: 10.1175/jpo-d-19-0064.1.

714 Tiago S. Dotto, Alberto C. Naveira Garabato, Anna K. Wåhlin, Sheldon Bacon, Paul R. Holland, Satoshi
715 Kimura, Michel Tsamados, Laura Herraiz-Borreguero, Ola Kalén, and Adrian Jenkins. Control of the oceanic
716 heat content of the getz-dotson trough, antarctica, by the amundsen sea low. *Journal of Geophysical Research:
717 Oceans*, 125(8), aug 2020. doi: 10.1029/2020jc016113.

718 Pierre Dutrieux, Jan De Rydt, Adrian Jenkins, Paul R. Holland, Ho Kyung Ha, Sang Hoon Lee, Eric J. Steig,
719 Qinghua Ding, E. Povl Abrahamsen, and Michael Schröder. Strong sensitivity of pine island ice-shelf melting
720 to climatic variability. *Science*, 343(6167):174–178, jan 2014. doi: 10.1126/science.1244341.

721 L. Favier, G. Durand, S. L. Cornford, G. H. Gudmundsson, O. Gagliardini, F. Gillet-Chaulet, T. Zwinger, A. J.
722 Payne, and A. M. Le Brocq. Retreat of pine island glacier controlled by marine ice-sheet instability. *Nature
723 Climate Change*, 4(2):117–121, jan 2014. doi: 10.1038/nclimate2094.

724 Raffaele Ferrari and Maxim Nikurashin. Suppression of eddy diffusivity across jets in the southern ocean.
725 *Journal of Physical Oceanography*, 40(7):1501–1519, jul 2010. doi: 10.1175/2010jpo4278.1.

726 Nathan P. Gillett, John C. Fyfe, and David E. Parker. Attribution of observed sea level pressure trends to
727 greenhouse gas, aerosol, and ozone changes. *Geophysical Research Letters*, 40(10):2302–2306, may 2013. doi:
728 10.1002/grl.50500.

729 Rishav Goyal, Alex Sen Gupta, Martin Jucker, and Matthew H. England. Historical and projected changes
730 in the southern hemisphere surface westerlies. *Geophysical Research Letters*, 48(4), feb 2021. doi:
731 10.1029/2020gl090849.

732 Karen Heywood, Louise Biddle, Lars Boehme, Pierre Dutrieux, Michael Fedak, Adrian Jenkins, Richard Jones,
733 Jan Kaiser, Helen Mallett, Alberto Naveira Garabato, Ian Renfrew, David Stevens, and Benjamin Webber.
734 Between the devil and the deep blue sea: The role of the amundsen sea continental shelf in exchanges between
735 ocean and ice shelves. *Oceanography*, 29(4):118–129, dec 2016. doi: 10.5670/oceanog.2016.104.

736 Paul Holland, Gemma O'Connor, Thomas Bracegirdle, Pierre Dutrieux, Kaitlin Naughten, Eric Steig, David
737 Schneider, Adrian Jenkins, and James Smith. Anthropogenic and internal drivers of wind changes over the
738 amundsen sea, west antarctica, during the 20th and 21st centuries. jul 2022. doi: 10.5194/tc-2022-121.

739 Paul R. Holland, Thomas J. Bracegirdle, Pierre Dutrieux, Adrian Jenkins, and Eric J. Steig. West antarctic ice
740 loss influenced by internal climate variability and anthropogenic forcing. *Nature Geoscience*, 12(9):718–724,
741 aug 2019. doi: 10.1038/s41561-019-0420-9.

742 Stan Jacobs, Adrian Jenkins, Hartmut Hellmer, Claudia Giulivi, Frank Nitsche, Bruce Huber, and Raul
743 Guerrero. The amundsen sea and the antarctic ice sheet. *Oceanography*, 25(3):154–163, sep 2012. doi:
744 10.5670/oceanog.2012.90.

745 Stanley S. Jacobs. On the nature and significance of the antarctic slope front. *Marine Chemistry*, 35(1-4):9–24,
746 nov 1991. doi: 10.1016/s0304-4203(09)90005-6.

747 Stanley S. Jacobs, Hartmut H. Hellmer, and Adrian Jenkins. Antarctic ice sheet melting in the southeast
748 pacific. *Geophysical Research Letters*, 23(9):957–960, may 1996. doi: 10.1029/96gl00723.

749 Adrian Jenkins, Pierre Dutrieux, Stan Jacobs, Eric Steig, Hilmar Gudmundsson, James Smith, and Karen Hey-
750 wood. Decadal ocean forcing and antarctic ice sheet response: Lessons from the amundsen sea. *Oceanography*,
751 29(4):106–117, dec 2016. doi: 10.5670/oceanog.2016.103.

752 Adrian Jenkins, Deb Shoosmith, Pierre Dutrieux, Stan Jacobs, Tae Wan Kim, Sang Hoon Lee, Ho Kyung Ha,
753 and Sharon Stammerjohn. West antarctic ice sheet retreat in the amundsen sea driven by decadal oceanic
754 variability. *Nature Geoscience*, 11(10):733–738, aug 2018. doi: 10.1038/s41561-018-0207-4.

755 Ian Joughin, Benjamin E. Smith, and Brooke Medley. Marine ice sheet collapse potentially under way for the
756 thwaites glacier basin, west antarctica. *Science*, 344(6185):735–738, may 2014. doi: 10.1126/science.1249055.

757 Satoshi Kimura, Adrian Jenkins, Heather Regan, Paul R. Holland, Karen M. Assmann, Daniel B. Whitt,
758 Melchoir Van Wessem, Willem Jan van de Berg, Carleen H. Reijmer, and Pierre Dutrieux. Oceanographic
759 controls on the variability of ice-shelf basal melting and circulation of glacial meltwater in the amundsen
760 sea embayment, antarctica. *Journal of Geophysical Research: Oceans*, 122(12):10131–10155, dec 2017. doi:
761 10.1002/2017jc012926.

762 J. M. Klinck and M. S. Dinniman. Exchange across the shelf break at high southern latitudes. *Ocean Science*,
763 6(2):513–524, may 2010. doi: 10.5194/os-6-513-2010.

764 W. G. Large, J. C. McWilliams, and S. C. Doney. Oceanic vertical mixing: A review and a model with a
765 nonlocal boundary layer parameterization. *Reviews of Geophysics*, 32(4):363, 1994. doi: 10.1029/94rg01872.

766 Carlos Moffat, Robert C. Beardsley, Breck Owens, and Nicole van Lipzig. A first description of the antarctic
767 peninsula coastal current. *Deep Sea Research Part II: Topical Studies in Oceanography*, 55(3-4):277–293, feb
768 2008. doi: 10.1016/j.dsr2.2007.10.003.

769 Mathieu Morlighem. MEaSURES BedMachine Antarctica, Version 2. *NASA National Snow and Ice Data*
770 *Center Distributed Active Archive Center*, 2020. doi: 10.5067/E1QL9HFQ7A8M.

771 J. Mouginot, E. Rignot, and B. Scheuchl. Sustained increase in ice discharge from the amundsen sea embay-
772 ment, west antarctica, from 1973 to 2013. *Geophysical Research Letters*, 41(5):1576–1584, mar 2014. doi:
773 10.1002/2013gl059069.

774 Kaitlin A. Naughten, Paul R. Holland, Pierre Dutrieux, Satoshi Kimura, David T. Bett, and Adrian Jenkins.
775 Simulated twentieth-century ocean warming in the amundsen sea, west antarctica. *Geophysical Research*
776 *Letters*, 49(5), mar 2022. doi: 10.1029/2021gl094566.

777 Hsien-Wang Ou. Watermass properties of the antarctic slope front: A simple model. *Journal of Physical*
778 *Oceanography*, 37(1):50–59, jan 2007. doi: 10.1175/jpo2981.1.

779 Alek A. Petty, Daniel L. Feltham, and Paul R. Holland. Impact of atmospheric forcing on antarctic continental
780 shelf water masses. *Journal of Physical Oceanography*, 43(5):920–940, may 2013. doi: 10.1175/jpo-d-12-
781 0172.1.

782 H. D. Pritchard, S. R. M. Ligtenberg, H. A. Fricker, D. G. Vaughan, M. R. van den Broeke, and L. Padman.
783 Antarctic ice-sheet loss driven by basal melting of ice shelves. *Nature*, 484(7395):502–505, apr 2012. doi:
784 10.1038/nature10968.

785 M. N. Raphael, G. J. Marshall, J. Turner, R. L. Fogt, D. Schneider, D. A. Dixon, J. S. Hosking, J. M. Jones,
786 and W. R. Hobbs. The amundsen sea low: Variability, change, and impact on antarctic climate. *Bulletin of*
787 *the American Meteorological Society*, 97(1):111–121, jan 2016. doi: 10.1175/bams-d-14-00018.1.

788 E. Rignot, J. Mouginot, M. Morlighem, H. Seroussi, and B. Scheuchl. Widespread, rapid grounding line retreat
789 of pine island, thwaites, smith, and kohler glaciers, west antarctica, from 1992 to 2011. *Geophysical Research*
790 *Letters*, 41(10):3502–3509, may 2014. doi: 10.1002/2014gl060140.

791 Eric Rignot, Jonathan L. Bamber, Michiel R. van den Broeke, Curt Davis, Yonghong Li, Willem Jan van de
792 Berg, and Erik van Meijgaard. Recent antarctic ice mass loss from radar interferometry and regional cli-
793 mate modelling. *Nature Geoscience*, 1(2):106–110, jan 2008. doi: 10.1038/ngeo102.

794 Ryan Schubert, Andrew F. Thompson, Kevin Speer, Lena Schulze Chretien, and Yana Bebieva. The antarctic
795 coastal current in the bellingshausen sea. *The Cryosphere*, 15(9):4179–4199, sep 2021. doi: 10.5194/tc-15-
796 4179-2021.

797 A. Shepherd, E. Ivins, E. Rignot, B. Smith, M. van den Broeke, I. Velicogna, P. Whitehouse, et al. Mass balance
798 of the antarctic ice sheet from 1992 to 2017. *Nature*, 558(7709):219–222, jun 2018. doi: 10.1038/s41586-018-
799 0179-y.

800 Paul Spence, Stephen M. Griffies, Matthew H. England, Andrew McC. Hogg, Oleg A. Saenko, and Nicolas C.
801 Jourdain. Rapid subsurface warming and circulation changes of antarctic coastal waters by poleward shifting
802 winds. *Geophysical Research Letters*, 41(13):4601–4610, jul 2014. doi: 10.1002/2014gl060613.

803 Andrew L. Stewart and Andrew F. Thompson. Connecting antarctic cross-slope exchange with southern ocean
804 overturning. *Journal of Physical Oceanography*, 43(7):1453–1471, jul 2013. doi: 10.1175/jpo-d-12-0205.1.

805 Andrew L. Stewart, Andreas Klocker, and Dimitris Menemenlis. Acceleration and overturning of the antarctic
806 slope current by winds, eddies, and tides. *Journal of Physical Oceanography*, 49(8):2043–2074, aug 2019. doi:
807 10.1175/jpo-d-18-0221.1.

808 Malte Thoma, Adrian Jenkins, David Holland, and Stan Jacobs. Modelling circumpolar deep water intrusions
809 on the amundsen sea continental shelf, antarctica. *Geophysical Research Letters*, 35(18), sep 2008. doi:
810 10.1029/2008gl034939.

811 Andrew F. Thompson, Andrew L. Stewart, Paul Spence, and Karen J. Heywood. The antarctic slope current
812 in a changing climate. *Reviews of Geophysics*, 56(4):741–770, dec 2018. doi: 10.1029/2018rg000624.

813 Andrew F. Thompson, Kevin G. Speer, and Lena M. Schulze Chretien. Genesis of the antarctic slope current
814 in west antarctica. *Geophysical Research Letters*, 47(16), aug 2020. doi: 10.1029/2020gl087802.

- 815 R. Timmermann, A. Le Brocq, T. Deen, E. Domack, P. Dutrieux, B. Galton-Fenzi, H. Hellmer, A. Humbert,
816 D. Jansen, A. Jenkins, et al. A consistent data set of antarctic ice sheet topography, cavity geometry, and
817 global bathymetry. *Earth System Science Data*, 2(2):261–273, dec 2010. doi: 10.5194/essd-2-261-2010.
- 818 Dzig P. Walker, Mark A. Brandon, Adrian Jenkins, John T. Allen, Julian A. Dowdeswell, and Jeff Evans.
819 Oceanic heat transport onto the amundsen sea shelf through a submarine glacial trough. *Geophysical Research*
820 *Letters*, 34(2), jan 2007. doi: 10.1029/2006gl028154.
- 821 Dzig P. Walker, Adrian Jenkins, Karen M. Assmann, Deborah R. Shoosmith, and Mark A. Brandon. Oceano-
822 graphic observations at the shelf break of the amundsen sea, antarctica. *Journal of Geophysical Research:*
823 *Oceans*, 118(6):2906–2918, jun 2013. doi: 10.1002/jgrc.20212.
- 824 Benjamin G. M. Webber, Karen J. Heywood, David P. Stevens, and Karen M. Assmann. The impact of
825 overturning and horizontal circulation in pine island trough on ice shelf melt in the eastern amundsen sea.
826 *Journal of Physical Oceanography*, 49(1):63–83, jan 2019. doi: 10.1175/jpo-d-17-0213.1.
- 827 Weifeng Zhang and Steven J. Lentz. Wind-driven circulation in a shelf valley. part II: Dynamics of the along-
828 valley velocity and transport. *Journal of Physical Oceanography*, 48(4):883–904, apr 2018. doi: 10.1175/jpo-
829 d-17-0084.1.